Acoustic phonon tunneling in $LiNbO_3$

Master's thesis, 3.6.2024

Author:

Toivo Hakanen

Supervisor:

Prof. Ilari Maasilta, Zhuoran Geng

UNIVERSITY OF JYVÄSKYLÄ
DEPARTMENT OF PHYSICS

Abstract

Hakanen, Toivo
Acoustic phonon tunneling in $LiNbO_3$
Master's thesis
Department of Physics, University of Jyväskylä, 2024, 71 pages.

In this thesis, the patterning techniques of lithium-niobate-on-insulator silicon chips were investigated to create free-standing membrane platforms of $LiNbO_3$ (lithium niobate) that are separated by a submicron gap for cryogenic acoustic phonon tunneling measurements. A three-layer mask of mr-PosEBR - Al_2O_3 - Cr was utilized in $LiNbO_3$ dry etching to achieve good gap edge quality. An estimated Cr to $LiNbO_3$ selectivity of 0.3 was achieved with an estimated $LiNbO_3$ etch rate of 6 nm/min and edge wall verticality of 56°. HF vapor was used to etch SiO_2 from underneath $LiNbO_3$ and release membrane platforms from bulk, and evaporated Al_2O_3 was used to protect devices from unwanted corrosion. Vapor etch had a SiO_2 etch rate of 0.5 μm/min, which is much higher than values found in literature. Ultimately, sample fabrication failed because the Al_2O_3 coating on top of membranes didn't protect the measurement devices fabricated on top of $LiNbO_3$ platforms from HF corrosion. Numerical calculations showed that the heat flux from the acoustic phonon tunneling is the strongest in the crystallographic X-direction, with a value of 5.2 $\mu W/m^2$ for two semi-infinite plates separated by a 200 nm gap at 0.1 K. Heat fluxes in the Y- and Z-directions were 5.0 $\mu W/m^2$ and 2.1 $\mu W/m^2$, respectively, under the same conditions. A similar trend was observed with tunneled power transmittance in the Y- and Z-directions: the Y-direction had higher power transmittance across all incident mode-tunneled mode pairs compared to the Z-direction.

Keywords: phonon tunneling, acoustic phonons, piezoelectricity, lithium niobate, $LiNbO_3$

Tiivistelmä

Hakanen, Toivo
Akustisten fononien tunnelointi $LiNbO_3$:ssa
Pro gradu -tutkielma
Fysiikan laitos, Jyväskylän yliopisto, 2024, 71 sivua

Tässä Pro Gradu -tutkielmassa tutkittiin piisirun eristeen päälle kasvatetun litiumniobaattikerroksen (LNOI, lithium-niobate-on-insulator) kuviointitekniikoita. Kuviontitekniikoilla oli tarkoitus valmistaa itseään kannattelevia alustoja $LiNbO_3$-kalvoista alle mikrometrin levyisen raon erottamana, joilla voisi tehdä kryogenisiä mittauksia akustisten fononien tunneloinnista. $LiNbO_3$ kuivaetsauksessa käytettiin kolmikerroksista mr-PosEBR - Al_2O_3 - Cr -kovaetsausmaskia, jolla saavutettiin hyvä raon reunan jälki. $LiNbO_3$ etsauksen selektiivisyyden arvioitiin olevan 0,3 Cr suhde $LiNbO_3$ reseptillä, minkä $LiNbO_3$ etsausnopeudeksi arvoitiin 6 nm/min ja reunan seinän kaltevuudeksi 56°. $LiNbO_3$ alustat vapautettiin SiO_2-kontaktista etsaamallla SiO_2 HF-höyryetsauksella. Höyrystettyä Al_2O_3 käytettiin suojaamaan sirulle rakennettuja mittalaiteita korroosiolta. HF-höyry etsasi SiO_2 0,5 μm/min nopeudella, mikä on huomattavasti nopeampaa kuin mitä kirjallisuudesta löytyy. Loppujen lopuksi mitattavien näytteiden valmistus epäonnistui siihen, että suojaava Al_2O_3-kerros ei oikeasti suojannut $LiNbO_3$-alustojen päälle rakennettuja mittalaitteita HF-korroosiolta. Numeeriset laskelmat osoittivat, että tunneloituvien fononien lämpövuo on voimakkaimmillaan kristallografisessa X-suuntaan. Lämpövuo oli 5,2 $\mu W/m^2$ kahdelle puoliäärettömälle kappaleelle 200 nm raon erottamana 0,1 K lämpötilassa. Lämpövuot Y- ja Z-suunnissa olivat vastaavasti 5,0 $\mu W/m^2$ ja 2,1 $\mu W/m^2$ samoissa olosuhteissa. Samanlainen trendi havaittiin tunneloituvien fononien siirtämällä teholla Y- ja Z-suunnissa: tunneloituneet fononit siirsivät enemmän tulevien fononien tehoa Y-suunnassa Z-suuntaan verrattuna.

Avainsanat: fononitunnelointi, akustiset fononit, pietsosähköinen ilmiö, litiumniobaatti, $LiNbO_3$

Preface

I would like to thank Prof. Ilari Maasilta and Dr. Zhuoran Geng for all of the guidance I received during this thesis. With their help, I could go as far as I could with the experimental and numerical work and complete the thesis within the tight schedule.

I would also like to thank all research group members present during the work, especially Mr. Aki Ruhtinas and Mr. Tatu Korkiamäki for the friendly work environment. The casual conversations in the cryogenics lab and especially Mr. Tatu Korkiamäki's help with the SINIS-junctions is greatly appreciated. I would like to thank Dr. Kimmo Kinnunen and Mr. Tarmo Suppula for their help with the cooling of the old RIE and for all the work done to keep the cleanroom operational. I would also like to thank everyone I have worked with in the cleanroom for their help and flexibility on reservations.

Lastly, I would like to thank my family for their support and my friends for the relaxing pastime and memories made during this work.

Jyväskylä, June 2024

Toivo Hakanen

Contents

1 Introduction

The continuous rise in both quantity and computing power of consumer electronics' is largely due to the technology industry's efforts to uphold Moore's Law. Moore's Law, an observation made by Gordon Moore in 1965, states that the number of transistors on a microchip doubles approximately every two years, leading to exponential growth in computing power. However, since the 2010s, this progress has slowed, prompting some experts to declare Moore's Law invalid. Despite this, the ongoing densification of transistors in integrated circuits will eventually face a critical challenge: heat dissipation. As transistors become smaller and more densely packed, the generated heat increases, which already set a practical clock limit to CPU [1].

Traditionally, heat dissipation in integrated circuits relies on the good thermal conductivity of bulk silicon to transfer heat away from the transistors to the backside of the silicon chip. The chip is then cooled further by adding a heat sink to the backside that exchanges excess heat to the air, which is then carried away through convection. However, these heat transfer mechanisms based on physical contact might not be sufficient to cool vertically stacked sheets of transistors, which is an option to uphold Moore's law when transistor size has met its limit. Moreover, smaller transistors operate in a domain where continuum physics does not apply, making the thermal resistance of different material interfaces even more significant[2]. This necessitates the investigation of alternative heat transfer mechanisms.

One interesting way to circumvent heat resistance is to utilize contactless heat transfer mechanisms, the most known of which is far-field photon radiation. However, when two surfaces are close enough, photons can tunnel directly to the neighboring surface, enhancing heat transfer. This is known as near-field radiative heat transfer (NFRHT) and it is a much stronger effect than black-body radiation (ideal far-field radiation) when the two surfaces are separated by a distance shorter than the dominant photon wavelength. NFRHT could be used to cool hotspots in integrated circuits, and its feasibility has been demonstrated in recent studies[3, 4]

Another contactless heat transfer mechanism, less known than far- or near-field photon radiation, is acoustic phonon tunneling in piezoelectric solids. Acoustic

phonons in any solid are quantum mechanical descriptions of propagating elastic vibrations[5, 6]. The piezoelectric effect induces an electric field from almost any deformation to the solid. This allows acoustic phonon tunneling by transforming phonons into electric fields that travel across the vacuum gap and transform back into phonons in the neighboring solid[7]. Phonons carry the heat of the solid's lattice and, in dielectrics they are the main heat carriers.

Acoustic phonon tunneling could be utilized in new transistor designs based on piezoelectric semiconductors, known as piezotronics. Piezotronic transistors are two-terminal devices, unlike the three-terminal conventional transistors. These devices use polarization induced by strain from the piezoelectric effect as a gate voltage. These transistors are unlikely to replace conventional transistors in computing, as current piezotronic devices are limited to MHz range clock speeds compared to GHz range in traditional transistors [8]. However, these transistors will most likely see usage in completely new type of devices due to the capability of directly responding to mechanical stimuli[8].

In this work, we investigate acoustic phonon tunneling in lithium niobate ($LiNbO_3$ or LN). Lithium niobate boasts strong coupling between electric and elastic fields, suggesting it would have stronger tunneling effects than aluminum nitride (AlN), as measured in a recent study[7]. Calculations of flux and transmitted power are presented to predict which crystal configuration is best for tunneling. Different fabrication methods of lithium-niobate-on-insulator (LNOI) were explored to realize a sample on which the hypothesis could be tested.

2 Elastic waves in piezoelectric media

Heat is understood at its most abstract form as thermal energy that is transferred from one system to another due to temperature difference between the two systems. Thermal energy in matter is kinetic energy of vibrating atoms and kinetic energy exchanged in collisions of atoms. In solid matter, atoms can vibrate collectively in a way that these collective vibrations can be described as free waves travelling inside the matter. These waves are quasi-particles known as phonons, which serve the role of wave quanta for mechanical waves, much like photons are the quanta of electromagnetic fields.

To study heat transport phenomena of vibrations of solid material, continuum anisotropic linear elasticity theory is used as the main theoretical framework for this thesis. Continuum physics assumes that material can be treated as a continuous volume rather than a discrete collection of atoms, which results in that variables such as density or Young's modulus can be treated as continuous averages of the underlying microscopic structure. Also, due to the nature of the studied material, anisotropicity has to be taken into account. Lastly linear elasticity assumes that material returns to its original shape and size after deformation and that said deformations are small enough that Hooke's law can be used to linearily relate strain and deformation of material to stress and internal traction force of solid.

2.1 Acoustic phonons from elasticity theory

In this section basic elastic equations from elasticity theory are used to explain phonons without the presence of piezoelectricity. This section is also used to establish notation conventions used in this work and to serve as an introduction to the piezoelectric theory, as it requires and understanding of both the elastic and the electromagnetic fields.

2.1.1 Elastic equations

Displacement $\boldsymbol{u}$ can be defined, when moving a volume element out of its equilibrium position $\boldsymbol{r}$ to new position $\boldsymbol{l}$, as a difference between the old and the new position,

$$\boldsymbol{u}(\boldsymbol{r}, t) = \boldsymbol{l}(\boldsymbol{r}, t) - \boldsymbol{r}. \tag{1}$$

Both $\boldsymbol{u}(\boldsymbol{r}, t)$ and $\boldsymbol{l}(\boldsymbol{r}, t)$ depend on time t to be able to handle time-dependent phenomena, such as vibrations, and on $\boldsymbol{r}$ to have a location dependence. Bolding is used here to designate both vectors and tensors, which in $\boldsymbol{u}$ case is a 1×3 column vector

$$\boldsymbol{u} = \begin{bmatrix} u_x \\ u_y \\ u_z \end{bmatrix}.$$

Sometimes index notation u_i will be used for easier calculation, in which case index i is used to go through all indexes x, y and z in the calculation.

However, it is evident that rigid translations and rotations are also covered by the displacement. This is not desirable, because vibrations happen only in situations where material is deformed, when its volume elements are out of equilibrium. Translations can be avoided with differential displacement $\mathrm{d}u_i = \mathrm{d}l_i - \mathrm{d}r_i$, although rotations are still included in $\mathrm{d}u_i$. Rotations can be excluded by only considering the scalar value of differential displacement. For that reason deformation is conventionally defined as

$$\Delta_d = \mathrm{d}l^2 - \mathrm{d}r^2. \tag{2}$$

With deformation, $\mathrm{d}l_i$ can be solved from differential displacement and then used with the chain rule to change $\mathrm{d}u_i$ to $\mathrm{d}r_i$ and to represent deformation with the strain tensor S_{ij}

$$\Delta_d = \mathrm{d}r_i S_{ij} \mathrm{d}r_j, \tag{3}$$

where $S_{ij} = (\nabla_j u_i + \nabla_i u_j + \sum_k \nabla_i u_k \nabla_j u_k)/2$. Notation $\nabla_i u_j = \partial u_j / \partial r_i$ is a shorthand for partial derivatives. Summation of repeated indices is applied to the above equation and and also applied to all future equations.

Voigt notation can be used to simplify strain assuming displacements are small enough for the quadratic terms to become negligible. With the linear strain approximation the strain tensor $S_{ij} = (\nabla_j u_i + \nabla_i u_j)/2$ has off-diagonal symmetry and can

Subscript L	Expression ij
1	xx
2	yy
3	zz
4	yz, zy
5	xz, zx
6	yx, xy

Table 1. Voigt notation translation rules to pair of ij.

be written in terms of Voigt notation convention as a six-element column vector

$$S_L = \nabla_{Lj} u_j. \tag{4}$$

The Voigt notation is explained in detail in Ref. [9], but Voigt indices are written in capital letters I,J,K and L instead of a,b,c and d to make a greater distintion to regular indices. The Voigt indices run through index pairs of i and j with translation rules shown in Table 1. From this convention the new 3×6 differential operator ∇_{Lj} reads as

$$\nabla_{Lj} = \begin{bmatrix} \partial/\partial r_x & 0 & 0 \\ 0 & \partial/\partial r_y & 0 \\ 0 & 0 & \partial/\partial r_z \\ 0 & \partial/\partial r_z & \partial/\partial r_y \\ \partial/\partial r_z & 0 & \partial/\partial r_x \\ \partial/\partial r_y & \partial/\partial r_x & 0 \end{bmatrix}. \tag{5}$$

Similarly, with the Voigt convention and linear elasticity approximation, the stress tensor σ is symmetric [10] and Hooke's law for stress-strain relation can be written as

$$\sigma_K = c_{KL} S_L. \tag{6}$$

Here elastic stiffness tensor c_{KL} is really a fourth-order tensor that linearly maps between the two second-order tensors, strain tensor S_L and stress tensor σ_K. Capital subscripts K and L are Voigt indices running from 1 to 6. Stress can also be related to displacement through the equation of motion for displacements [7]

$$\nabla_{iK} \sigma_K = \rho \frac{\partial^2 u_i}{\partial t^2} - F_i^V. \tag{7}$$

In this equation, ρ is the material mass density and F_i^V is a body force that can act directly to the volume elements within objects, and is in units of N/m^3. Velocity $\boldsymbol{v} = \partial \boldsymbol{u}/\partial t$ with the Voigt convention reads satisfies the matrix equation

$$\nabla_j v_{jL} = \frac{\partial}{\partial t}(\nabla_{Lj} u_j) = \frac{\partial S_L}{\partial t}. \tag{8}$$

2.1.2 Acoustic phonons

Usually vibrations are not bound to a fixed place, but are waves of collective lattice vibrations travelling across the studied medium. In such case it is useful to introduce the general plane wave solution

$$\boldsymbol{u} = \sum_{\alpha} \boldsymbol{A}_\alpha e^{-i\boldsymbol{k}\cdot\boldsymbol{r}+i\omega t} \tag{9}$$

for the equation of motion, Eq. (7). The presented solution for a moving displacement field $\boldsymbol{u}$ is a sum of three acoustic bulk wave modes α, which have displacement amplitudes $\boldsymbol{A}_\alpha$ in different directions orthogonal to each other, also called polarizations. Each wave mode has a wave vector $\boldsymbol{k}$ designating the traveling direction for the wave and a frequency ω. In Eq. (9) there is also imaginary unit i and time t. It should be noted that in piezoelectric media there are more modes than just the three acoustic bulk modes.

The waves of collective vibrations (9) describes are commonly known as phonons. More accurately phonons are the quantized vibrations in solid media,[5, 6] similar to photons being quantized electromagnetic waves. However, photons are elementary particles that can be measured directly, whereas phonons are quasiparticles that do not exist on their own without a matter medium.

Phonons can be classified into two categories: acoustic and optical. For crystalline structures, there are always three basic acoustic modes, and $3n - 3$ optical modes for $n \geq 2$, where n is the amount of atoms in the primitive cell of the crystal.[11] However, optical modes are disregarded here as they can not be explained by elasticity theory. To predict optical phonons theory needs to able to differentiate atoms inside the unit cell and as elasticity theory treats matter as continuous, the theory is not capable of predicting existence of optical phonons. This omission is not a problem for low-temperature studies, where optical phonons are not excited at all due their high frequency range[11].

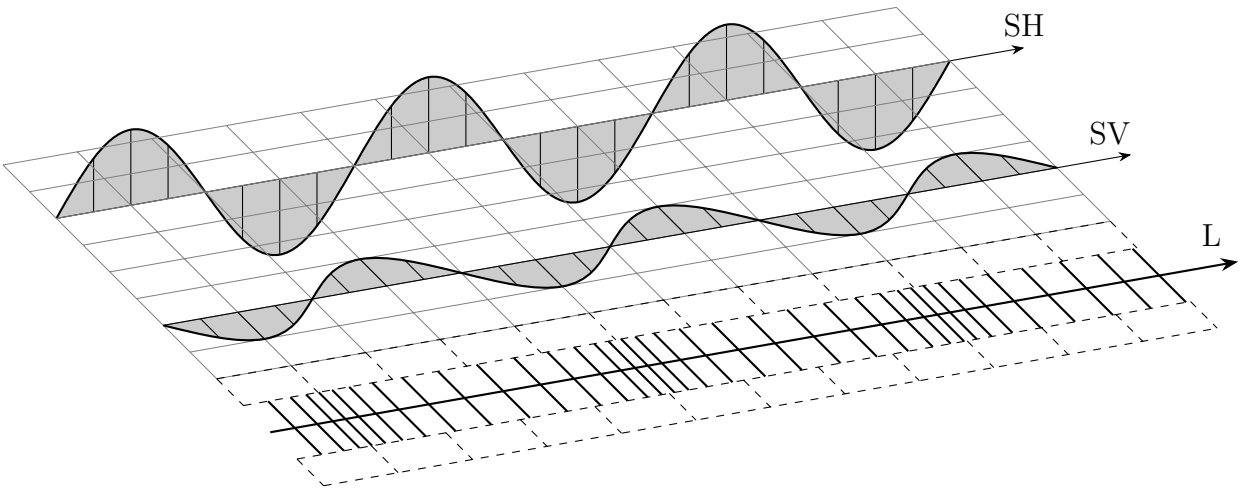

Figure 1. Illustration of acoustical bulk waves. SV and SH stand for vertical shear and horizontal shear, respectively.

Bulk waves for acoustic phonons consist of three different polarizations[10, 11], where all three waves are orthogonal to each other in terms of polarization direction and any other wave can be represented as a linear combination of them, as is in Eq. (9). The most common way of identifying the bulk waves is separating them by their polarizations: one longitudinal (L) and two transverse waves (SV, SH), which can be seen in Fig. 1. Transverse waves are also known as shear waves. Longitudinally polarized waves are similar to pressure waves, where the vibration of the medium happens in the same direction as the wave vector $\boldsymbol{k}$. For transverse waves the polarization is orthogonal to $\boldsymbol{k}$. In isotropic media the phase velocity of the transverse waves would be degenerate[10] and therefore indistinguishible from each other by velocity alone. However, in anistropic media the two shear wave modes are not degenerate and also in most cases, the polarization of bulk waves are not purely longitudinal or transverse, but are quasimodes of mixed character, which reduce to pure bulk waves only in certain conditions. These quasimodes are neither completely orthogonal (quasishear) nor completely parallel (quasilongitudinal) to their respective wave vectors. In this work it is to be assumed that the waves are quasimodes with the exception of special symmetry directions in some configurations where pure wave modes can exist.

In this work, bulk waves are sorted with the phase velocity $|\boldsymbol{v}| = \omega/|\boldsymbol{k}|$ convention instead of identifying modes from polarizations. With the velocity convention waves are identified by their wave velocity from fastest to slowest mode, the first

being quasilongitudinal(L), then the fast quasitransverse(FT) and finally the slow quasitransverse wave(ST). In computational calculations, this is the more efficient and simple method for the mode identification.

2.1.3 Christoffel matrix and slowness surface

Taking the plane waves (9) into account, the following differential operators can be simplified $\nabla_j \rightarrow -ik_j$, $\nabla_{Lj} \rightarrow -ik_{Lj}$ and $\frac{\partial}{\partial t} \rightarrow i\omega$ due to $\nabla_j u_j = -ik_j u_j$ and $\frac{\partial}{\partial t} u_j = i\omega u_j$. In Voigt notation, wave matrix $k_{Lj} = (k_{iK})^T$ is of the same form as Eq. (5), just with k_i as elements instead of $\partial/\partial r_i$. Assuming a sourceless material with the bodyforce $\boldsymbol{F}^V$ set to zero, Eq. (7) can then be written as an eigenvalue problem using the stress-strain (6) and strain-displacement (4) relations

$$\begin{aligned} & -ik_{iK}\sigma_K = -\rho\omega^2 u_i \\ \iff \quad & -i^2 k_{iK} c_{KL} k_{Lj} u_j = \rho\omega^2 u_i \\ \iff \quad & (k^2\Gamma_{ij} - \rho\omega^2\delta_{ij})u_j = 0. \end{aligned} \tag{10}$$

The derived equation (10) is known as the Christoffel equation and subsequently $\Gamma_{ij} = k_{iK} c_{KL} k_L j/k^2$ is known as the Christoffel matrix. A short-hand for vector norm $\sqrt{\sum_j k_j^2} = k$ is used for less obfuscated equations. The dispersion relation $\omega = \boldsymbol{v}(\boldsymbol{n}) \cdot \boldsymbol{k}$, where $\boldsymbol{v}(\boldsymbol{n})$ is the propagation direction dependent phase velocity, and $\boldsymbol{n} = \boldsymbol{k}/k$ is the wave normal, can then be obtained by setting the characteristic determinant $|k^2\Gamma_{ij} - \rho\omega^2\delta_{ij}| = 0$ to zero. The relation can be expressed in terms of k/ω resulting in the so called slowness (or inverse velocity $1/\boldsymbol{v_p}$) surface, which is a characteristic of a material.

Slowness surfaces can be used to gain insight in the crystal plane at hand. At a first glance a,slowness surface simply tells how fast the acoustic wavefronts can travel in a particular direction when angular frequency is kept constant. This information can also be used for a geometric approach to scattering problems from plane interfaces, as such scattering processes have to conserve the velocity component parallel to the scattering plane. This is demonstrated graphically in Fig. 4, which shows how mode conversions could take place, and predicts the reflection and refraction angles for each mode. This approach also demonstrates that slower modes with incident angles θ_i larger than critical angles θ_c cannot scatter into faster waves. In Figure 4 if the slow transverse mode(green dotted line) has incident angle $\theta_i > \theta^{ST}$ then

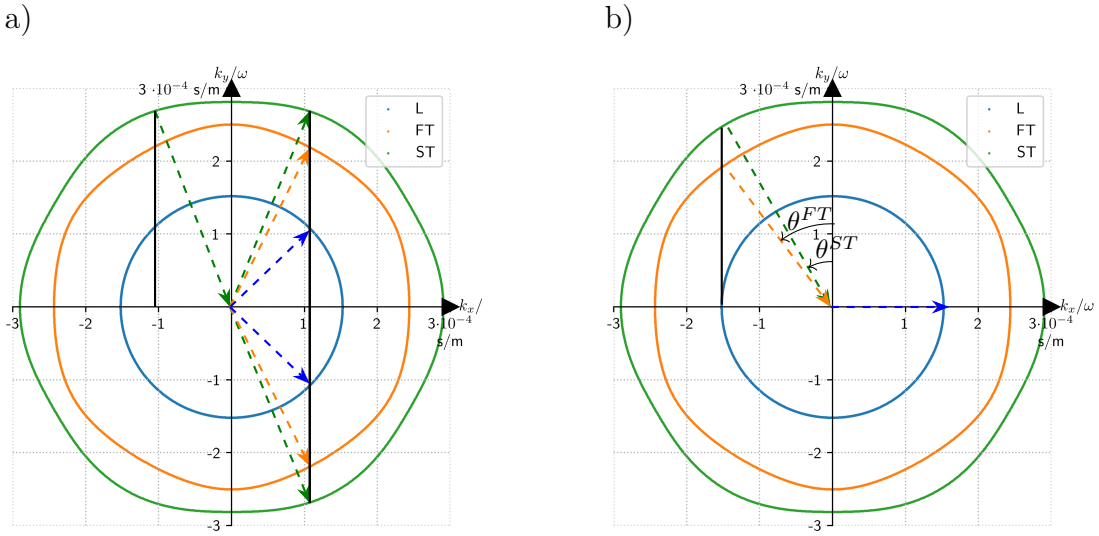

Figure 2. Slowness surface of Z-cut $LiNbO_3$ with the piezoelectric effect ignored, see Sec. 3.1 and Fig. 6 for more information about $LiNbO_3$ crystal surfaces. In the picture a) incident slow transverse wave is shown scattering back to positive y side of x axis from a scattering interface coinciding with the x-axis, or transmitting through the interface to negative y side. In b) the critical incident angles of the slow transverse mode to the longitudinal mode θ^{ST} and the fast transverse mode to the longitudinal mode θ^{FT} are shown. Black solid vertical lines are a guide to the eye, signifying that the k_x component is conserved in the scattering process.

the black solid vertical line wouldn't cross the slowness curve of the longitudinal mode(blue dotted line) and the slow transverse mode cannot excite the longitudinal mode anymore.

2.1.4 Complex acoustic Poynting Vector

Displacement fields describing plane waves are usually written in complex notation, and that affects the expression for the acoustic Poynting vector, describing acoustic power flow. Deriving the complex vector is similar to a real Poynting vector, therefore the complex derivation is presented here because the complex vector is more relevant. With the complex conjugate of v_j and equality [10, 7]

$$\nabla_j(v_{jL}^*\sigma_L) = \frac{\partial u_j^*}{\partial t}(\nabla_{jL}\sigma_L) + \sigma_L(\nabla_j v_{jL}^*) \tag{11}$$

the divergence theorem can be applied on the left hand side after integrating both sides over volume V. Then inserting Equation (7) and multiplying each term by 1/2 we end up with an equation

$$\oint_S \frac{1}{2}(-v_{jL}^*\sigma_L)n_j \mathrm{d}S = \frac{1}{2}\int_V -v_j^*\rho\frac{\partial^2 u_j}{\partial t^2} - \sigma_L \nabla_{Lj}\frac{\partial u_j^*}{\partial t}\ \mathrm{d}V + \frac{1}{2}\int_V \frac{\partial u_j^*}{\partial t}F_j^V \mathrm{d}V$$
$$= i\omega\int_V \frac{1}{2}\sigma_L S_L^* - \frac{1}{2}\rho\left(\frac{\partial^2 u_j}{\partial t^2}\right)^2\ \mathrm{d}V + i\omega\int_V -\frac{1}{2}u_j^* F_j^V \mathrm{d}V. \quad (12)$$

The above equation signifies the conservation of the power flow inside a volume V. By using the relation $v_j = \partial u_j/\partial t$, Equation (8) and the plane wave solutions for derivatives of the displacement $\partial u_j/\partial t = i\omega$ and $\partial u_j^*/\partial t = -i\omega$, the volume integrals can be simplified in Eq. (12). Now the integrands can be identified [10] as the Poynting vector $\boldsymbol{P}$, the peak stored kinetic energy density $(\mathrm{u}_K)_{\mathrm{peak}}$, the peak stored elastic energy density $(\mathrm{u}_S)_{\mathrm{peak}}$ and the power generated from body force P_s:

$$\boldsymbol{P} = -\frac{1}{2}\boldsymbol{v}^* \cdot \boldsymbol{\sigma}, \quad (13)$$

$$(\mathrm{u}_K)_{\mathrm{peak}} = \frac{\rho}{2}\left(\frac{\partial \boldsymbol{u}}{\partial t}\right)^2, \quad (14)$$

$$(\mathrm{u}_S)_{\mathrm{peak}} = \frac{1}{2}\boldsymbol{\sigma} \cdot \boldsymbol{S}^*, \quad (15)$$

$$P_s = -\frac{1}{2}\boldsymbol{u}^* \cdot \boldsymbol{F}^V. \quad (16)$$

Media studied in this work are assumed to be source free. Therefore the body force $F^V = 0$ and thus the source power $P_s = 0$. Furthermore, with the assumption of a lossless medium, the energy velocity of wave $\boldsymbol{v}_e$ is equal to group velocity of wave $\boldsymbol{g}$, [10] and thus the group velocity can be written in terms of the time averaged power flow and average stored energy density [7, 10] as

$$\boldsymbol{g} = \frac{2\boldsymbol{P}_{\mathrm{AV}}}{(\mathrm{u}_K)_{\mathrm{peak}} + (\mathrm{u}_S)_{\mathrm{peak}}}, \quad (17)$$

where $\boldsymbol{P}_{\mathrm{AV}} = -\frac{1}{2}\mathrm{Re}(\boldsymbol{v}^* \cdot \boldsymbol{\sigma})$ is the real part of complex Poynting vector describing the time-averaged power flow.

2.2 Piezoelectricity

Piezoelectricity is a complex phenomenon that combines elastic and electric response together. Materials that generate electric potential in response to changes in strain are called piezoelectric, because in its most simplest form such materials generate voltage when pressed, which is aptly described by the greek word "piezo" meaning "to press". However, the phenomenon also includes stretching the material for an inverse electrical response, and also strains induced by introducing a electric potential to the material. Due to these properties, piezoelectric materials are ideal transducers for transforming sound to electrical signal and vice versa.

The piezoelectric constitutive stress equations result from the coupling of the elastic fields with the electric field $\boldsymbol{E}$. [10] This coupling affects both stress tensor $\boldsymbol{\sigma}$ and electric displacement $\boldsymbol{D}$

$$\sigma_K = c_{KL}^E S_L - e_{Kj} E_j \tag{18}$$

$$D_i = e_{iL} S_L + \epsilon_{ij}^S E_j. \tag{19}$$

In the Equations above c_{KL}^E is the stiffness tensor at constant electric field, denoted by upper index E, and ϵ_{ij}^S is the electric permittivity tensor at constant strain, denoted by upper index S. Piezoelectric stress tensors e_{Kj} and e_{iL} are the same tensor due to symmetry requirements[7], just with different indexing. The piezoelectic stress tensor signifies the strength of the coupling, and if all of the tensor elements were 0, the material would not be piezoelectric and the Equations (18) and (19) would decouple from each other.

Considering only quasistatic electric fields that satisfy $\boldsymbol{E} = -\nabla\Phi$ and by using the plane wave approximation with Gauss's law $\nabla \cdot \boldsymbol{D} = -ik_i D_i = 0$, from Eq. (19) we can solve the electric potential field Φ

$$\Phi = \frac{k_i e_{iL} k_{Lj}}{k_i \epsilon_{ij}^S k_j} u_j. \tag{20}$$

With the solved Φ, $\boldsymbol{E}$ can be eliminated from Eq. (18), and that equation can then be inserted to the equation of motion (7) with $F_i^V = 0$, to finally obtain

$$k_{iK}\left[c_{KL}^E + (e_{Kj}k_j)\frac{(k_i e_{iL})}{k_i \epsilon_{ij}^S k_j}\right] k_{Lj} u_j = \rho\omega^2 u_i. \tag{21}$$

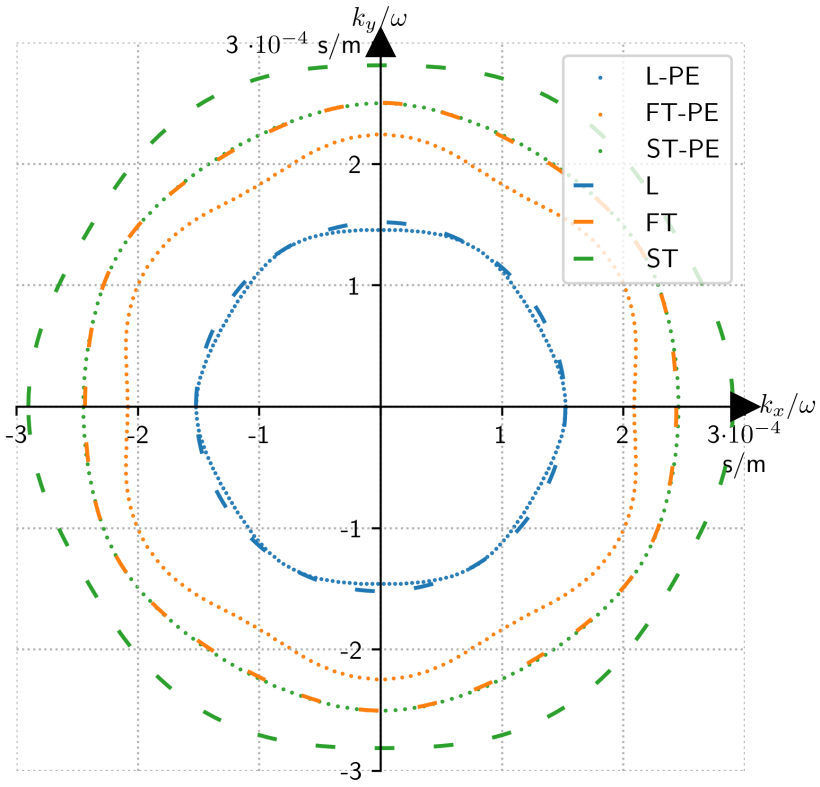

Figure 3. Slowness surfaces of $LiNbO_3$ Z-cut plotted with the piezoelectric effect (dotted) using Eq. (22) and without it (dashed) using Eq. (10). The piezoelectric stiffening can be seen from the general shrinking trend of the slowness curves for each mode. See Sec. 3.1 and Fig. 6 for more information about $LiNbO_3$ crystal surfaces.

The above equation can be written in a more familiar way

$$(k^2\Gamma_{ij}^{\mathrm{PE}} - \rho\omega^2\delta_{ij})u_j = 0, \tag{22}$$

where $\Gamma_{ij}^{\mathrm{PE}} = \frac{1}{k^2}k_{iK}\left[c_{KL}^{E} + \frac{(e_{Kj}k_j)(k_i e_{iL})}{k_i\epsilon_{ij}^{S}k_j}\right]k_{Lj}$ is the piezoelectrically stiffened Christoffel matrix [10]. With this equation the slowness surfaces of materials can be plotted, while taking the piezoelectric effect into account, see Fig. 3.

The piezoelectric effect on the Poynting vector is somewhat simpler, as the acoustic and electromagnetic vectors can just be summed together as $\boldsymbol{P}^{\mathrm{PE}} = \boldsymbol{P}^{\mathrm{acoustic}} + \boldsymbol{P}^{\mathrm{EM}}$. In this case $\boldsymbol{P}^{\mathrm{acoustic}}$ is the piezoelectrically stiffened Poynting vector. However,

by looking deeper into the well known complex electromagnetic Poynting vector $\boldsymbol{P}^{\mathrm{EM}} = \boldsymbol{E} \times \boldsymbol{H}^*/2$ within the quasistatic approximation it can be shown that the electromagnetic contribution doesn't affect the expression for the group velocity, Eq. (17). H in $\boldsymbol{P}^{\mathrm{EM}}$ is the magnetic field strength, and taking divergence on the Poynting vector gives

$$\nabla \cdot \boldsymbol{P}^{\mathrm{EM}} = (\nabla \times \boldsymbol{E}) \cdot \boldsymbol{H}^* - \boldsymbol{E} \cdot (\nabla \times \boldsymbol{H}^*). \tag{23}$$

The first term with the $\nabla \times \boldsymbol{E}$ rotor on the right hand side is zero, due to quasistatic approximation leaving out rotational parts of the field. The second term can be further expanded using Ampere's law $\nabla \times \boldsymbol{H}^* = \partial \boldsymbol{D}^*/\partial t$, the quasistatic approximation $\boldsymbol{E} = -\nabla\Phi$ and the divergence product rule $\nabla \cdot (\Phi \frac{\partial \boldsymbol{D}^*}{\partial t}) = (\nabla\Phi) \cdot \frac{\partial \boldsymbol{D}^*}{\partial t} + \Phi\nabla \cdot \frac{\partial \boldsymbol{D}^*}{\partial t}$ to end up with

$$\nabla \cdot \boldsymbol{P}^{\mathrm{EM}} = -\frac{1}{2}\nabla \cdot \left(\Phi \frac{\partial \boldsymbol{D}^*}{\partial t}\right) + \frac{1}{2}\Phi\nabla \cdot \frac{\partial \boldsymbol{D}^*}{\partial t}. \tag{24}$$

The second term can be eliminated, which is zero due to Gauss's law. Lastly, it can be seen that the equation is symmetrically operated by the divergence operator which can then be removed to finally arrive at a simple expression for the EM Poynting vector

$$\boldsymbol{P}^{\mathrm{EM}} = -\frac{1}{2}\Phi \frac{\partial \boldsymbol{D}^*}{\partial t}. \tag{25}$$

It can be seen that as the power flow contributions of elastic and electromagnetic properties are additive, doing the volume integral over the piezoelectric Poynting vector will result in the same peak stored energy densities, Eqs. (14) and (15), and only results in a new term for the peak stored electrostatic energy density

$$(\mathrm{u}_E)_{\mathrm{peak}} = i\Phi k_i D_i^*/2, \tag{26}$$

which is zero for bulk waves due to Gauss's law. As nothing changed in regards to the peak stored energy densities, the Eq. (17) remains unchanged. It should be noted that while the expression of group velocity didn't change in the Eq. (17), it is still affected by the piezoelectric components in the piezoelectric stress (18), piezoelectrically stiffened phase velocities and the electromagnetic power flow in the time-averaged power flow $\boldsymbol{P}_{\mathrm{AV}}$.

2.3 Piezoelectricity with Stroh formalism

It is possible to solve piezoelectric problems with the standard formulation presented in the previous section and to handle scattering and tunneling problems in the scope of this work, but it is extremely heavy computationally. Solving scattering problems with Christoffel matrices requires building the matrices for both sides of the scattering boundary, and solving for the fields self-consistently that matches the incoming and outgoing modes.

The theoretical framework for phonon tunneling is based on the extended Stroh formalism[12, 13]. This section will mainly just highlight the most important parts to understand and study the tunneling phenomenon, the full derivations and orthonormalization procedures are found in Ref. [7]. We start from general plane wave solutions regarding displacement, electric potential, stress and electric displacement [7]:

$$\begin{aligned} p_\alpha &= \frac{k_z}{k_x} \\ \boldsymbol{u} &= \sum_\alpha b_\alpha \boldsymbol{A}_\alpha e^{-ik_x(x+p_\alpha z)+i\omega t} \\ \Phi &= \sum_\alpha b_\alpha \phi_\alpha e^{-ik_x(x+p_\alpha z)+i\omega t} \\ \boldsymbol{n}\cdot\boldsymbol{\sigma} &= ik_x \sum_\alpha b_\alpha \boldsymbol{L}_\alpha e^{-ik_x(x+p_\alpha z)+i\omega t} \\ \boldsymbol{n}\cdot\boldsymbol{D} &= ik_x \sum_\alpha b_\alpha D^n_\alpha e^{-ik_x(x+p_\alpha z)+i\omega t}, \end{aligned} \tag{27}$$

where b_α is the dimensionless amplitude of the partial wave mode α. The constants containing units for the partial wave modes are $\boldsymbol{A}_\alpha$ for the displacement, ϕ_α for the electric potential, $\boldsymbol{L}_\alpha$ for the traction force and D^n_α for the normal projection of the electric displacement. The equations are set up in a way that fields vary only in xz-plane, which is known as the plane of incidence. Alongside fixed coordinates, Eqs. (27) assume that wave vectors are contained in the xz-plane such that waves with $k_z < 0$ are moving towards the scattering interface and the interface lies in the xy-plane. In this setup all waves have a zero y-component, $k_y = 0$, and k_x is considered a conserved quantity in scattering processes. Unit vectors $\boldsymbol{n}$ and $\boldsymbol{m}$ coincide with the z-axis and the x-axis, respectively. Finally a factor the $p_\alpha = k_z/k_x$ is defined to be the ratio of the two $\boldsymbol{k}$-vector components in the observation coordinates.

In the Stroh formalism, the set of above variables can be neatly packed into a

single Stroh characteristic eigenequation for the partial wave mode α [7]

$$\boldsymbol{N}(v_x)\xi_\alpha = p_\alpha \xi_\alpha. \tag{28}$$

In the equation, the normalized eigenvectors $\xi_\alpha = [\boldsymbol{A}_\alpha, \phi_\alpha, \boldsymbol{L}_\alpha, D^n_\alpha]^T$ contains all the information on the partial wave modes from the set of Eq. (27) . The Stroh matrix reads as

$$\boldsymbol{N}(v_x) = -\begin{bmatrix} (\boldsymbol{nn})^{-1}(\boldsymbol{nm}) & (\boldsymbol{nn})^{-1} \\ (\boldsymbol{mn})(\boldsymbol{nn})^{-1}(\boldsymbol{nm}) - (\boldsymbol{mm}) + \rho v_x^2 \boldsymbol{I'} & (\boldsymbol{mn})(\boldsymbol{nn})^{-1} \end{bmatrix}, \tag{29}$$

which is an eight dimensional matrix with four dimensional composite matrix entries. The composite matrices are formed with the following formula:

$$(\boldsymbol{nm}) \equiv \begin{bmatrix} n_{iK} & 0 \\ 0 & n_i \end{bmatrix} \begin{bmatrix} c^E_{KL} & e_{Kj} \\ e_{iL} & -\epsilon^S_{ij} \end{bmatrix} \begin{bmatrix} m_{Lj} & 0 \\ 0 & m_j \end{bmatrix}. \tag{30}$$

As with other matrices with indices similar to Kj, $n_{Lj} = (n^T_{iK})$ and $m_{Lj} = (m^T_{iK})$ are of the similar form as ∇_{Lj} from Eq. (5). Lastly, the $\boldsymbol{I'}$ matrix reads as

$$\boldsymbol{I'} = \begin{bmatrix} 1 & 0 & 0 & 0 \\ 0 & 1 & 0 & 0 \\ 0 & 0 & 1 & 0 \\ 0 & 0 & 0 & 0 \end{bmatrix}, \tag{31}$$

As the composite matrices only contain material constants such as the stiffness, the piezoelectric stress and the electric permittivity, the x-component of the phase velocity from the incident wave can be considered to be the sole variable in the Stroh matrix. Furthermore, phase velocities can be computed quite easily from piezoelectrically stiffened Christoffel matrix (22) using the aforementioned material constants and the incident angle of the wave as the input. This means that full knowledge of the waves can be calculated just from incident angle of the wave, assuming that the material parameters are known.

2.3.1 Phonon tunneling with scattering approach

All of the previous theory in this thesis so far has only been explaining how acoustic vibrations work inside solid matter and how they couple to the electric field in piezoelectric matter. However, acoustic phonon tunneling requires the examining of what happens at the boundary between solid and vacuum, in the vacuum between the solids and again at the boundary between vacuum and the second solid. Here we review the main aspects of the recently developed general theory for phonon tunneling across vacuum [14, 7]. Vacuum is considered, as the existence of any matter between the solids would lead to dominance of conventional heat transfer mechanisms that have been studied well. These boundaries are expressed in the boundary conditions

$$\begin{aligned} \Phi^{(i)} &= \Phi_V \\ \boldsymbol{n} \cdot \boldsymbol{D}^{(i)} &= \boldsymbol{n} \cdot \boldsymbol{D}_V \\ \boldsymbol{n} \cdot \boldsymbol{\sigma}^{(i)} &= \boldsymbol{0}, \end{aligned} \tag{32}$$

where the upper index $(i) = 1{,}2$ is used to differentiate between the two solids involved in tunneling and the lower index V denotes fields that exist in vacuum. The conditions in short require continuity of the electric potential and the normal component of the electric displacement at the solid-vacuum interface, and that the solid at the boundary is a mechanically free surface.

The presence of vacuum in the boundary conditions gives rise to new solutions for the electric potential and the electric displacement. In vacuum, the electric potential has to satisfy the Laplace equation $\nabla^2 \Phi_V = 0$, which in the chosen coordinates leads to $(k_x^2 + k_z^2)\Phi_V = 0$ and more explicitly to $k_z = \pm i k_x$ for plane waves. This gives rise to the solution for electric potential in vacuum

$$\Phi_V = (b_{V+}\phi_{V+}e^{k_x z} + b_{V-}\phi_{V-}e^{-k_x z})e^{i\omega t - ik_x x}. \tag{33}$$

With the coordinate setup, the incident and transmitted waves are travelling in the negative z direction, which makes the $V-$ term to be an exponentially increasing term in the solution. The common factor phase factor $e^{i\omega t - ik_x x}$ is going to be omitted in further derivations for simplicity.

For the electric displacement, the relation $\boldsymbol{D}_V = -\epsilon_0 \nabla \Phi_V$ can be used to write a

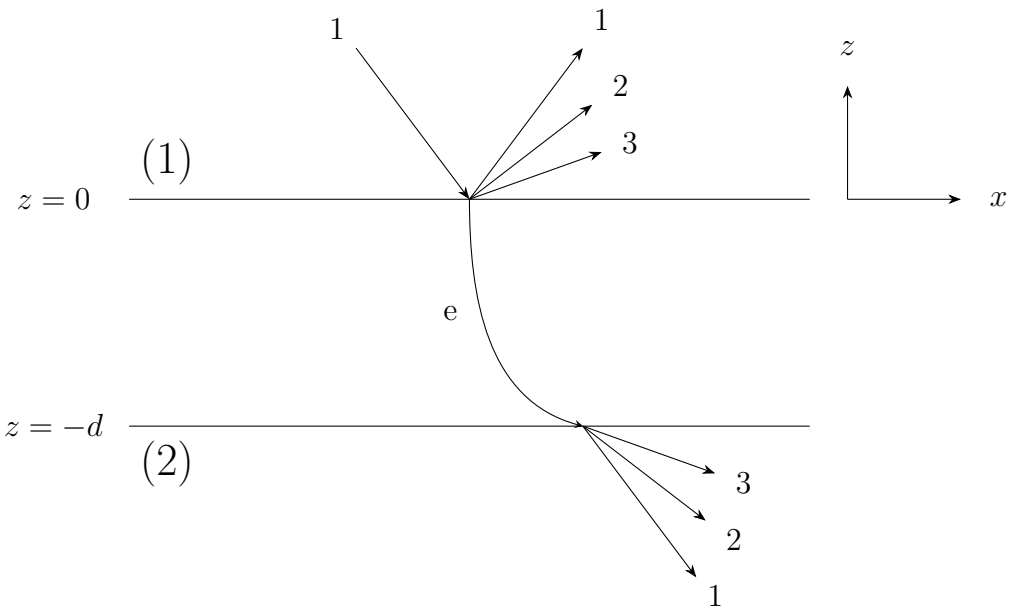

Figure 4. Illustrative example of the phonon tunneling problem. Mode 1 travelling in solid (1) scatters back into solid (1) as three different partial modes. The incident mode 1 can also transmit to vacuum as an exponentially decaying electical evanescent mode which can transmit the incident mode as the same set of the three partial modes to the solid (2). The e in vacuum stands for evanescent and the curved trajectory is to highlight the exponential decay of the mode. The interface of solid (1) is set as $z = 0$, and the interface solid (2) is set as the gap lenght d, $z = -d$. In this setup, transmission happens along the negative z direction.

solution for the electric displacement in vacuum using Eq. (33):

$$\boldsymbol{n}\cdot\boldsymbol{D}_V = -\epsilon_0 k_x b_{V+}\phi_{V+}e^{k_x z} + \epsilon_0 k_x b_{V-}\phi_{V-}e^{-k_x z}. \tag{34}$$

With these solutions and an introduction of a 5×1 column vector $\boldsymbol{U}_\gamma^{(i)} = [\phi_\gamma^{(i)}, D_\gamma^{n,(i)}, \boldsymbol{L}_\gamma^{(i)}]^T$, $(i) = 1,2$, $\gamma = \alpha,in$, the boundary conditions can be written more explicitly in a shorter form for solids (1) and (2):

$$\begin{aligned} b_{in}^{(1)}\boldsymbol{U}_{in}^{(1)} + \sum_{\alpha=1}^{4} b_\alpha^{(1)}\boldsymbol{U}_\alpha^{(1)} &= b_{V+}\boldsymbol{U}_{V+} + b_{V-}\boldsymbol{U}_{V-} \\ \sum_{\alpha=1}^{4} b_\alpha^{(2)} e^{ip_\alpha^{(2)}k_x d}\boldsymbol{U}_\alpha^{(2)} &= b_{V+}\boldsymbol{U}_{V+}e^{-k_x d} + b_{V-}\boldsymbol{U}_{V-}e^{k_x d}. \end{aligned} \tag{35}$$

In the above equations the interface of solid (1) is set to be at $z = 0$, and for solid (2) the interface is set to be at the gap width d, $z = -d$. With this coordinate setup $\exp(\pm k_x z) = 1$ in the incident wave boundary conditions. An illustrative example of the setup is shown in Fig. 4.

One way to approach the tunneling problem is to use a scattering matrix to connect the incoming modes from solid (1) to outgoing modes in solid (2). This can be done by noting that each phonon mode has its respective transmission and reflection amplitude coefficients on both surfaces of solids. These coefficients treat scattering processes in complete isolation and are called single surface coefficients[7]. For example, the scattering matrix for solid (1) can take into account incident wave transmitting into vacuum as $\bar{t}_{in\to V}^{(1)}$, incident wave reflecting back to solid (1) as one of the partial waves as $\bar{r}_{in\to 1}^{(1)}...\bar{r}_{in\to 4}^{(1)}$, the wave transmitting into solid (1) from vacuum as $\bar{t}_{V\to 1}^{(1)}...\bar{t}_{V\to 4}^{(1)}$ and lastly the vacuum wave transmitting back to vacuum from the surface of solid (1) as $\bar{r}_V^{(1)}$. The notation of lines over single surface constants are used to differentiate the constants from the total transmission and scattering coefficients. Now more generally, the scattering matrix for a surface of solid (i) $S^{(i)}$ can be written as a coupling between the incident and outgoing mode amplitudes

$$\begin{bmatrix} b_1^{(i)} \\ b_2^{(i)} \\ b_3^{(i)} \\ b_4^{(i)} \\ b_t^{(V)} \end{bmatrix} = S^{(i)} \begin{bmatrix} b_{in}^{(i)} \\ b_{in}^{(V)} \end{bmatrix} = \begin{bmatrix} \bar{\boldsymbol{r}}^{(\boldsymbol{i})} & \bar{\boldsymbol{t}}^{(\boldsymbol{i})} \\ \bar{t}_{in\to V}^{(i)} & \bar{r}_V^{(i)} \end{bmatrix} \begin{bmatrix} b_{in}^{(i)} \\ b_{in}^{(V)} \end{bmatrix}. \tag{36}$$

The superscript (V) denotes electric potential waves that exist in the vacuum gap. The column vectors $\bar{\boldsymbol{r}}^{(i)} = [\bar{r}^{(i)}_{in\to 1}...\bar{r}^{(i)}_{in\to 4}]^T$ and $\bar{\boldsymbol{t}}^{(i)} = [\bar{t}^{(i)}_{V\to 1}...\bar{r}^{(i)}_{V\to 4}]^T$ are collections of reflection coefficients inside solid (i) and transmission coefficients to solid (i) from the vacuum, respectively.

The boundary condition for solid (1), Eq. (35), can be rearranged to have all inputs on the right hand side and all outputs on the left hand side, similar to Eq. (36)

$$\begin{bmatrix} \boldsymbol{U}_1^{(1)} & \boldsymbol{U}_2^{(1)} & \boldsymbol{U}_3^{(1)} & \boldsymbol{U}_4^{(1)} & -\boldsymbol{U}_{V+} \end{bmatrix} \begin{bmatrix} b_1^{(i)} \\ b_2^{(i)} \\ b_3^{(i)} \\ b_4^{(i)} \\ b_{V+} \end{bmatrix} = \begin{bmatrix} -\boldsymbol{U}_{in}^{(1)} & \boldsymbol{U}_{V-} \end{bmatrix} \begin{bmatrix} b_{in}^{(1)} \\ b_{V-} \end{bmatrix}. \tag{37}$$

In the above equation $\begin{bmatrix} \boldsymbol{U}_1^{(1)} & \boldsymbol{U}_2^{(1)} & \boldsymbol{U}_3^{(1)} & \boldsymbol{U}_4^{(1)} & -\boldsymbol{U}_{V+} \end{bmatrix}$ is a 5×5 matrix, and assuming it is invertible, we can multiply above equation with the matrix inverse and end up with a matrix that connects input modes to output modes. The same can be done for the boundary conditions of solid (2) in Eq. (35), so that scattering matrices for both solid interfaces are constructed as

$$\begin{aligned} S^{(1)} &= \begin{bmatrix} \boldsymbol{U}_1^{(1)} & \boldsymbol{U}_2^{(1)} & \boldsymbol{U}_3^{(1)} & \boldsymbol{U}_4^{(1)} & -\boldsymbol{U}_{V+} \end{bmatrix}^{-1} \begin{bmatrix} -\boldsymbol{U}_{in}^{(1)} & \boldsymbol{U}_{V-} \end{bmatrix} \\ S^{(2)} &= \begin{bmatrix} \boldsymbol{U}_1^{(2)} & \boldsymbol{U}_2^{(2)} & \boldsymbol{U}_3^{(2)} & \boldsymbol{U}_4^{(2)} & -\boldsymbol{U}_{V-} \end{bmatrix}^{-1} \begin{bmatrix} -\boldsymbol{U}_{in}^{(2)} & \boldsymbol{U}_{V+} \end{bmatrix}. \end{aligned} \tag{38}$$

When the single surface coeffiecients are known, full transmission and reflection coefficients for each partial wave mode can be calculated. The total transmission coefficient can be understood with a multiple reflection picture. In this interpretation, the transmission of the incident wave mode as a partial wave mode α first requires the incident mode to transmit out of solid (1) to vacuum ($\bar{t}^{(1)}_{in\to V}$) as an evanescent electric potential wave. This wave partly transmits into solid (2) at the first contact ($\bar{t}^{(2)}_{V\to\alpha}$) after travelling across the gap once ($\exp(-k_x d)$), and partly reflects back to vacuum from solid (2), then partly reflects again from solid (1) to vacuum, after which it can transmit into solid (2) after travelling the gap thrice ($\exp(-3k_x d)$). This happens until the electric potential wave has transmitted back to either solid, part of it back to solid (1), and the rest transmitting over the gap to solid (2). This impinging of vacuum electric potential wave between the solids can thus be described

as a geometric series

$$\begin{aligned} t_\alpha =& \bar{t}^{(1)}_{in\to V} e^{-k_x d} \bar{t}^{(2)}_{V\to\alpha} + \bar{t}^{(1)}_{in\to V} \bar{r}^{(1)}_V \bar{r}^{(2)}_V e^{-3k_x d} \bar{t}^{(2)}_{V\to\alpha} \\ &+ \bar{t}^{(1)}_{in\to V} (\bar{r}^{(1)}_V)^2 (\bar{r}^{(2)}_V)^2 e^{-5k_x d} \bar{t}^{(2)}_{V\to\alpha} + ... \\ =& \frac{\bar{t}^{(1)}_{in\to V} \bar{t}^{(2)}_{V\to\alpha} e^{-k_x d}}{1 - \bar{r}^{(1)}_V \bar{r}^{(2)}_V e^{-2k_x d}}. \end{aligned}$$

A similar description can be made for the partial wave mode reflection to solid (1). Both reflection and transmission have a common multiple reflection coefficient

$$f_m(d) = \frac{e^{-k_x d}}{1 - \bar{r}^{(1)}_V \bar{r}^{(2)}_V e^{-2k_x d}}. \tag{39}$$

Now, the coupled transmission and reflection coeffiecients can be written out as

$$t_\alpha = \bar{t}^{(1)}_{in\to V} \bar{t}^{(2)}_{V\to\alpha} f_m(d) \tag{40}$$

$$r_\alpha = \bar{r}^{(1)}_\alpha + \bar{r}^{(2)}_V \bar{t}^{(1)}_{in\to V} \bar{t}^{(2)}_{V\to\alpha} f_m(d) e^{-k_x d}, \tag{41}$$

which tell how much of the incident wave converts into partial wave mode α through the reflection and transmission processes.

An alternative and equivalent way to calculate to calculate reflection and transmission amplitude coefficients is to take the ratio of the output mode amplitude with the incident amplitude from Eq. (35)

$$t_\alpha \equiv b^{(2)}_\alpha e^{ip^{(2)}_\alpha k_x d} / b^{(1)}_{in}, \quad r_\alpha \equiv b^{(1)}_\alpha / b^{(1)}_{in}. \tag{42}$$

This definition is more useful for the combined boundary condition approach to solve the tunneling problem, which is covered in more detail in Ref. [7].

2.3.2 Heat flux of tunneled phonons

This section will cover the formulation of general heat flux across a vacuum gap, if thermally average phonon radiation impinges on the solid vacuum interface[7, 14]. The coordinate system is divided into two sets of angles, two crystal rotation angles and two incident angles. The first crystal rotation is ψ rotation around the z-axis and the second rotaoin is ϑ around the x-axis. For incident angles, θ is the incident angle with respect to the z-axis in the plane of incidence (xz-plane of fixed

observation coordinates) and φ is the rotation of the plane of incidence around the z-axis. Crystal rotations are considered constants when calculating the flux, and fully new calculations are needed if the crystal configuration is changed. Note that up until this point, the presented theory has been built from the viewpoint of studying a single incident mode scattering on the solid-vacuum interface and the resulting partial wave modes were labeled as α. Now the total heat flux from tunneling requires summation of all contributing incident waves, which are going to be labeled as γ to differentiate them from partial wave modes in scattering processes.

The time-averaged power flow of the partial wave mode α normal to the solid-vacuum interface can be expressed as the normal projection of the real part of the Poynting vector [7]

$$P_\alpha^{(i)} \equiv \boldsymbol{n} \cdot \mathrm{Re}(\boldsymbol{P}_\alpha^{(i)}) = -\frac{\omega k_x}{4}|b_\alpha|^2 \boldsymbol{\xi}_\alpha^T \hat{\boldsymbol{T}} \boldsymbol{\xi}_\alpha^*, \tag{43}$$

where

$$\hat{\boldsymbol{T}} = \begin{bmatrix} \hat{O}_{(4)} & \hat{I}_{(4)} \\ \hat{I}_{(4)} & \hat{O}_{(4)} \end{bmatrix}. \tag{44}$$

The $\hat{O}_{(4)}$ and $\hat{I}_{(4)}$ matrices are 4×4 zero and identity matrices, respectively. $\boldsymbol{\xi}_\alpha^T \hat{\boldsymbol{T}} \boldsymbol{\xi}_\alpha^*$ is just ± 1 for the acoustic bulk modes with the units of force, and it can be used to determine the direction of the power flow. It is important to note that for evanescent waves $\boldsymbol{\xi}_\alpha^T \hat{\boldsymbol{T}} \boldsymbol{\xi}_\alpha^*$ is strictly zero to ensure a strong cut-off in power flow. As the magnitude of the power flow of the mode depends on the dimensionless amplitude b_α, using the second definition of the coupled transmission coefficient, Eq. (42), gives a simple relation between the incident and the transmitted power flow of a single partial wave mode

$$P_\alpha^{(2)} = |t_\alpha|^2 P_{in}^{(1)}. \tag{45}$$

The total power transferred over the vacuum gap is the sum over all transmitted partial wave modes, which can be expanded with Eq. (40) as $P_\Sigma^{(2)} = \sum_\alpha |\bar{t}_{in\to V}^{(1)} \bar{t}_{V\to\alpha}^{(2)} f_m(d)|^2 P_{in}^{(1)}$. For identical mediums in solid (1) and (2), we can use relations $\bar{r}_V \equiv \bar{r}_V^{(2)} = -\bar{r}_V^{(1)}$ and $2\mathrm{Re}(\bar{r}_V) = \sum_\alpha |\bar{t}_{V\to\alpha}^{(2)}|^2$ derived in Ref. [7, 15], to write the total power transmittance of the incident mode γ as

$$\mathcal{T}_\gamma(\theta,\varphi,k,d) = \frac{P_\Sigma^{(2)}}{P_\gamma^{(1)}} = \frac{2\mathrm{Re}(\bar{r}_V)|\bar{t}_{\gamma\to V}^{(1)}|^2 e^{-2kd\sin\theta}}{|1+\bar{r}_V^2 e^{-2kd\sin\theta}|^2}. \tag{46}$$

Total power transmittance is written above with a direct dependence on the incident angle θ in the plane of incidence and on the rotation angle ϕ of the plane of incidence around the z-axis. This rotation setup allows to take into account the full k-space. Overlined single surface coefficients also depend on the incident angles, but are not written as functions for the sake of simplicity.

The peak stored energy densities can be obtained from Eqs. (15), (14) and (26) and written more explicitly in terms of the general wave solutions used in Stroh formalism as

$$\begin{aligned}(\mathrm{u}_K)_{\mathrm{peak}} = (\mathrm{u}_S)_{\mathrm{peak}} &= 2^{-1}\rho\omega^2|b_\gamma|^2|\boldsymbol{A}_\gamma|^2 \\ (\mathrm{u}_E)_{\mathrm{peak}} &= 0.\end{aligned} \tag{47}$$

Now group velocity normal to the interface can be written more explicitly from Eq. (17)

$$g_\gamma^n \equiv \boldsymbol{n}\cdot\boldsymbol{g}_\gamma = -\frac{\sin\theta}{2\rho v_\gamma|\boldsymbol{A}_\gamma|^2}\boldsymbol{\xi}_\gamma^T\hat{\boldsymbol{T}}\boldsymbol{\xi}_\gamma^*. \tag{48}$$

Similarly to the power transmittance, only the component normal to the solid-vacuum interface is considered. In the Equation $k_x = k\sin\theta$ relation was used to bring out the angle dependence which was then further substituted with $\omega_\gamma = kv_\gamma$.

The energy carried by the incident thermal phonons is obtained from the average energy of Bose-Einstein statistics

$$\Pi(\omega,T) = \frac{\hbar\omega}{\exp(\hbar\omega/k_BT)-1}, \tag{49}$$

where $\hbar$ is the reduced Planck constant and k_B is the Boltzmann constant. At low enough temperatures where phonon tunneling is of any significance[7], the phonon dispersion relation can be considered linear and substitution $\omega_\gamma = kv_\gamma$ is used while calculating the flux.

The total heat flux of incident phonon modes γ that tunnel from solid (1) at temperature T to the adjacent solid (2) at 0 K can be in general written as an integral over full k-space and sum of all modes γ using the average energy $\Pi[\omega_\gamma(k),T]$ of phonons moving at group velocity $g_\gamma^n(\theta,\varphi)$ that transmit energy over the gap at the rate of transmittance $\mathcal{T}(\theta,\varphi,k,d)$:

$$J^{\mathrm{PE}}(T,d) = \sum_\gamma \int \Pi[\omega_\gamma(k),T]g_\gamma^n(\theta,\varphi)\Theta[-g_\gamma^n(\theta,\varphi)]\mathcal{T}_\gamma(\theta,\varphi,k,d)\frac{\mathrm{d}^3k}{(2\pi)^3}. \tag{50}$$

Using the earlier definitions of transmittance (46), group velocity (48), average energy (49) and with the spherical coordinates of k-space $\mathrm{d}^3k = k^2 \sin\theta \mathrm{d},\theta \mathrm{d}\varphi \mathrm{d}k$ the flux can be written explicitly as

$$\begin{aligned} J^{\mathrm{PE}}(T,d) = &- \frac{1}{8\pi^3\rho} \sum_{\gamma} \int_0^{2\pi} \mathrm{d}\varphi \int_0^{\pi} \mathrm{d}\theta \frac{\sin^2\theta}{|\boldsymbol{A}_\gamma|^2} \mathrm{Re}(\bar{r}_V) |\bar{t}^{(1)}_{\gamma\to V}|^2 \boldsymbol{\xi}_\gamma^T \hat{\boldsymbol{T}} \boldsymbol{\xi}_\gamma^* \Theta[\boldsymbol{\xi}_\gamma^T \hat{\boldsymbol{T}} \boldsymbol{\xi}_\gamma^*] \\ &\times \int_0^{\infty} \mathrm{d}k \frac{k^3}{\exp(v_\gamma \hbar k / k_B T) - 1} \frac{\exp(-2kd\sin\theta)}{|1 + \bar{r}_V^2 \cdot \exp(-2kd\sin\theta)|^2}. \end{aligned} \tag{51}$$

3 Numerical calculations of phonon tunneling

This section aims to illustrate phonon tunneling phenomena in $LiNbO_3$ and provide insights into which crystal orientations should be considered in sample fabrication. It also highlights the crystal structure and piezoelectric properties of $LiNbO_3$.

3.1 Properties of $LiNbO_3$

Lithium niobate ($LiNbO_3$) is a complex oxide composed of lithium and niobium, and it belongs to the trigonal crystal system with a 3m point group symmetry[16, 11]. This classification signifies a three-fold rotational symmetry against Z-axis (see. Fig 5), such that each 120°rotation leads to an identical configuration.The '3' in the 3m point group refers to this trigonal symmetry, while the 'm' indicates the presence of a mirror plane, dividing the crystal into two identical halves.

$LiNbO_3$ is inherently ferroelectric [16, 17]. Ferroelectricity, akin to ferromagnetism, refers to materials having a permanent polarization that can be reoriented by an external electric field, demonstrating a hysteresis loop effect. Ferroelectric materials are a subset of pyroelectric materials, which polarize due to temperature changes. Pyroelectric materials belong to 10 out of the 32 crystal point groups, all of which are also piezoelectric. $LiNbO_3$'s ferroelectric phase is very stable, with a Curie temperature of 1210°C, allowing it to remain ferroelectric even under harsh lithography conditions[18].

The crystallographic configuration of lithium niobate are conveniently described using a Cartesian coordinate system (X, Y, Z) aligned with the hexagonal real-space lattice directions ($\boldsymbol{t}_1$, $\boldsymbol{t}_2$, $\boldsymbol{t}_3$). Here, $\boldsymbol{t}_1$, $\boldsymbol{t}_2$, and $-\boldsymbol{t}_1$ $-\boldsymbol{t}_2$ lie in a plane separated by 120° angles, and $\boldsymbol{t}_3$ is orthogonal to this plane, corresponding to the crystal's *c*-axis. The Cartesian Z-axis coincides with the c-axis, the axis of rotational symmetry and spontaneous polarization. The X-axis is aligned with one of the hexagonal lattice vectors, and the Y-axis follows the right-hand rule.

$LiNbO_3$ can be described using either a hexagonal unit cell or a rhombohedral primitive cell. This work only considers the hexagonal unit cell, for which the four

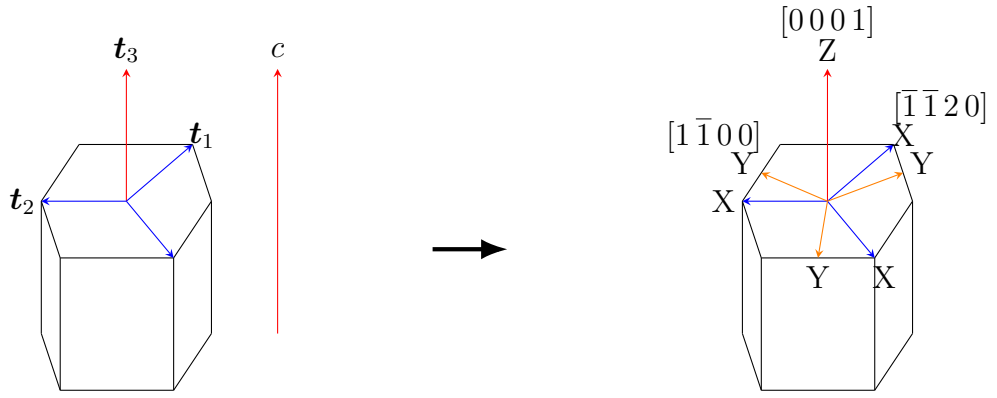

Figure 5. Basic hexagonal crystal vectors $\boldsymbol{t}_i$ and polarization axis c in a) and a Cartesian XYZ system fixed to it in b). X and Y-axes are threefold degenerate due to threefold rotatianol symmetry around Z-axis. Common convention is to fix X-axis to $[\bar{1}\,\bar{1}\,2\,0]$ direction and Y-axis to $[1\,\bar{1}\,0\,0]$ according to right hand rule.

index Bravais-Miller notation is used. Formula for translating three-index Miller notation into four-index *hkil* Bravais-Miller notation

$$(u,v,w) \rightarrow [2u - v, -u + 2v, -u - v, 3w] \tag{52}$$

translates equivalent X-axis vectors $(1\,0\,0)$, $(0\,1\,0)$ and $(1\,\bar{1}\,0)$ to $[2\,\bar{1}\,\bar{1}\,0]$, $[\bar{1}\,2\,\bar{1}\,0]$ and $[\bar{1}\,\bar{1}\,2\,0]$ hexagonal directions. The advantage of the Bravais-Miller notation is that equivalent directions can be found conveniently through permutations of *hki* indices. A clear example can be seen in $\langle\bar{1}\,\bar{1}\,2\,0\rangle$ equivalent directions of X-axis. Common convention is to fix X-axis to $[\bar{1}\,\bar{1}\,2\,0]$ and then Y-axis to $[1\,\bar{1}\,0\,0]$ following the right hand rule. Z-axis is translated to $[0\,0\,0\,1]$ direction. The crystal planes are referred by their surface normal axes, known as Z-cut for XY-plane, Y-cut for XZ-plane and X-cut for YZ-plane all of which are commercially available.

Z-cut has a static polarization of 0.7 C/m^2[19, 20, 21, 22] in its ferroelectric phase, which is among the highest found in ferroelectric materials. However the polarization in practice can be three orders of magnitude lower due to compensation mechanisms [23]. It is the only ferroelectric surface out of the three commercial cuts. Polarization sensing in the Z-direction can utilize either piezoelectric or pyroelectric properties of $LiNbO_3$[16]. Pressing the crystal along the $[0\,0\,0\,1]$ direction reverses the polarization of the +Z-face. In addition, the polarization in Z-axis will be enhanced upon cooling.

Y- and X-cuts are not ferroelectric like the Z-cut. Of the two, only the Y-cut is piezoelectric. The X-cut lacks piezoelectricity because the X-axis is perpendicular to the crystal's mirror plane, causing displacements in the X-axis direction to be compensated on the opposite side of the mirror plane, preventing polarization. The Y-cut, while nominally non-polar, is piezoelectric with a surface charge up to one-third of the Z-cut[21, 20].

All aforementioned crystal cuts are relevant for numerical study, as samples can be fabricated with tunneling gaps in the Z- or Y-cut orientations. X-cut is the thin film surface for the lithium-niobate-on-insulator silicon chips used in experiments. It is also included in the followed numerical demonstration for completeness.

3.2 Flux, and transmission and power coefficients

Phonon tunneling in $LiNbO_3$ was studied numerically using the theoretical framework outlined in Sec. 2 detailed further in [7, 14, 15]. Calculations involved solving the piezoelectrically stiffened Christoffel equation, Eq. (22) for incident phase velocities $\boldsymbol{v}_p$ using material tensors, the rotation of material parameters and the incident angle of waves as input. The x-component of these velocities in observer coordinates was then used as an input to solve the Stroh matrix in Eq. (29), from which the eigenvectors (ξ_α) and the eigenvalues (p_α) were calculated using Eq. (28). These were then used to calculate the total transmission coefficient t_α, Eq. (40), the power transmittance, Eq. (46) and the tunneling heat flux, Eq. (51), using multiple reflection approach, and electrically open and mechanically free boundary conditions. Anaconda Python distribution was used for numerical computations and graph plotting.

Calculation of the different crystal cuts was done by rotating the unrotated material parameters in $z-x-z$ rotation scheme, where the crystal is first rotated by ψ around z-axis, then by ϑ around x-axis and then by φ around z-axis a second time all according to right hand rule. The fixed observer coordinate system is denoted by the italic letters xyz, while the crystal configuration coordinates are denoted by the capital letters XYZ. In these coordinate systems the plane of incidence lies in the xz-plane, and only the crystal coordinates are rotated around fixed the x- and z-axes. An unrotated crystal would have its X- and Z-axes aligned with the x- and z-axis which matches to unrotated XY-plane (Z-cut) of the crystal. Any other cut is achieved by aligning the surface normal vector of the cut with the z-axis. Explicitly

	$LiNbO_3$
$c^E(10^{10}\ \mathrm{Nm}^{-2})$	
c_{11}	20.3
c_{33}	24.5
c_{44}	6
c_{66}	7.5
c_{12}	5.3
c_{13}	7.5
c_{14}	0.9
$e\ (\mathrm{Cm}^{-2})$	
e_{15}	3.7
e_{22}	2.5
e_{31}	0.2
e_{33}	1.3
$\epsilon^S\ (\epsilon_0)$	
ϵ_{xx}	44
ϵ_{zz}	29
Density ρ ($\mathrm{kg/m}^3$)	4700
Crystal class	$3m$

Table 2. $LiNbO_3$ material parameters used in numerical calculations. c^E is the stiffness tensor in constant electric field, e is piezoelectric stress tensor and ϵ^S is electric permittivity in constant strain. Values are from [10].

the XZ-plane (Y-cut) is from a $\vartheta = 90°$ rotation around the x-axis and the YZ-plane (X-cut) is from first rotating the crystal by $\psi = 90°$ around the z-axis and then rotating the crystal by another $\vartheta = 90°$ around the x-axis. To fully study each cut all cuts are scanned by a full $\varphi = 360°$ rotation around z-axis. Crystal cuts without the φ rotation are shown in Fig. 6.

Color maps of power transferred by transmitted partial wave mode P_α/P_{in} and partial wave mode transmission coefficient $|t_\alpha|$ were produced by plotting their strength against the incident angle and the surface normal rotation (φ rotation). All pairs of incident modes and transmitted partial wave modes were plotted for P_α/P_{in} and $|t_\alpha|$ for X- Y- and Z-cuts, which is 54 graphs in total. Only the most interesting graphs will be presented (see Figs. 7, 8). The range of input parameters for incident angle were from 0.1° start angle to 179.9° end angle with a 0.5° step, and for φ from angle of 0° to angle of 360° with a step of 1°. The chosen parameter range for incident angle ensured a finite k_x in calculations. The material parameters used are listed in Table 2.

Power transmittance patterns followed similar trends to $|t_\alpha|$, with sharp cutoffs at critical angles. This type of behaviour is expected, as the incident modes scattering into faster wave modes beyond their critical angles result in evanescent waves that decay exponentially[7]. Evanescent waves do not either carry power back into the bulk of the solid (1), or transmit power directly into the bulk of the second solid, as they cannot propagate in the z-direction. This also makes sense because $|t_\alpha|$ can be well over 1 (Fig. 7) due to its imaginary component beyond the critical angle in some incident angle - φ configurations.

The power transmittance across all incident mode - transmitted partial wave mode pairs in all cuts is generally stronger when the incident angles are closer to glancing angles around 60° to 90° degrees. This is because electric power flow is perpendicular to the wave propagation direction due to Gauss's law, and therefore electric power flow is more perpendicular to the solids surface and has a higher chance of transmitting power. The effect is commonly more pronounced with incident angles slightly larger than the critical angle to transmit as the faster mode. This is in agreement with [7] and due to faster modes reflecting as "surface wave like" evanescent waves and thus concentrating the respective power flow of slower modes near critical angles, introducing a strong electric field leaking into vacuum. This happens only with FT to FT, ST to FT and ST to ST transmissions. In addition, each incident

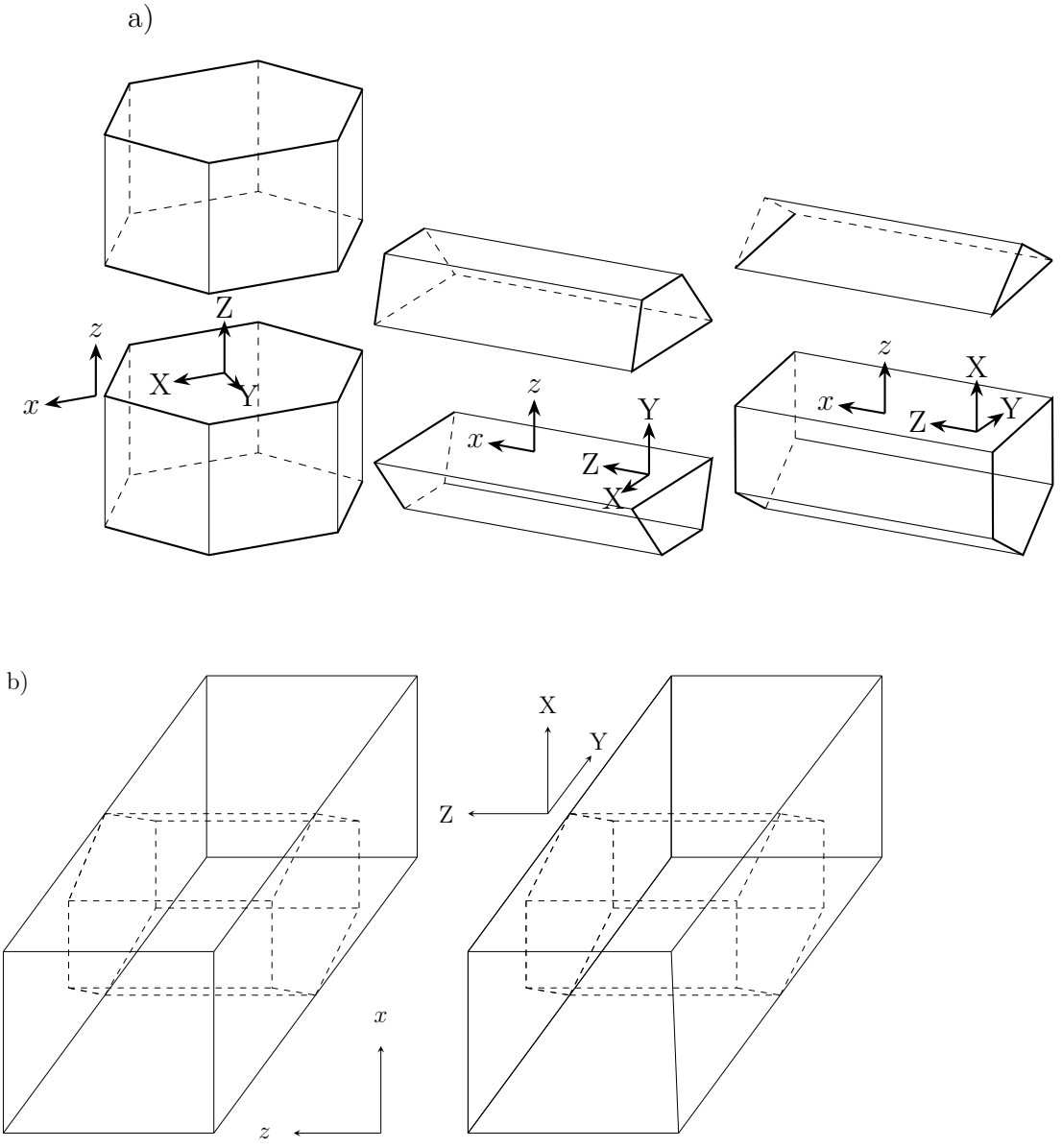

Figure 6. a) Visualisation of different crystal cuts. Z-cut is on the left which is an unrorated crystal. Y-cut is on the middle with $\vartheta = 90°$ rotation and on the right is X-cut from $\psi = 90°, \vartheta = 90°$ rotations done in the listed order. b) Illustration of the Z-cut tunneling gap in X-cut thin film. The solid line boxes are part of the X-cut thin film, and the dashed line highlights the cystal inside the thin film.

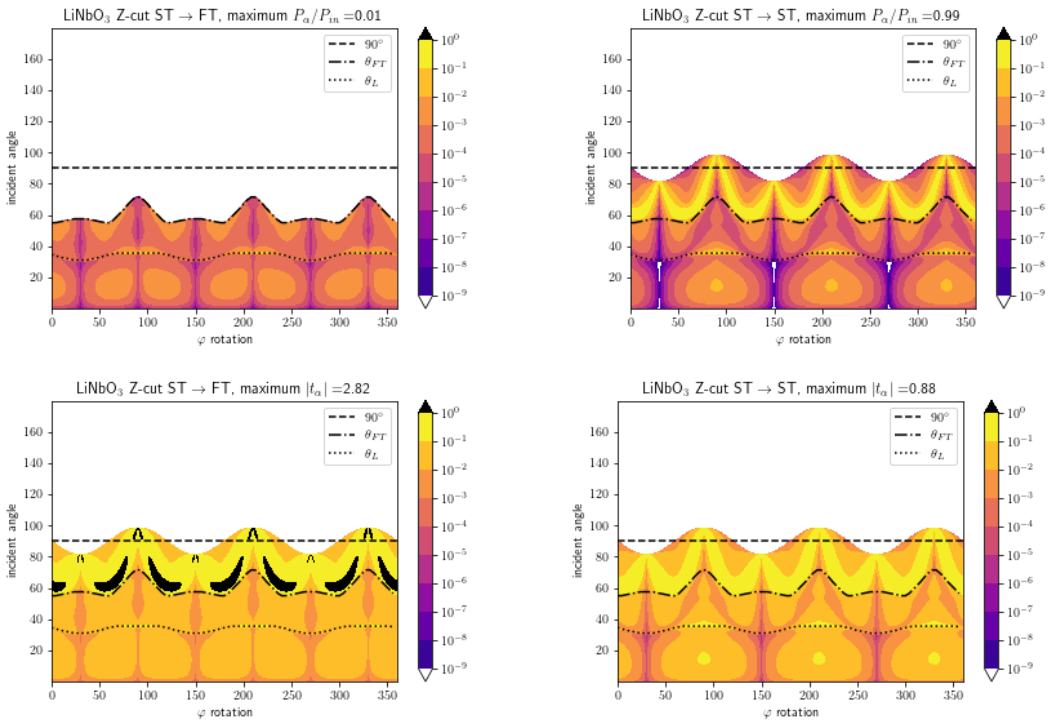

Figure 7. Relation between power transmittance (upper panels) and transmission coefficient (lower panels) plots. In the upper left panel power transmittance cuts off at the critical angle, even though there is still transmission in the lower left panel for the same configuration of Z-cut and incident ST mode transmitting as FT mode. On the right there is no cut off for ST mode transmitting as ST mode and power transmittance matches the shape of transmission coefficient plot. Also power transmittance on the right is significantly stronger for incident angles beyond the critical angle for FT mode θ_{FT}.

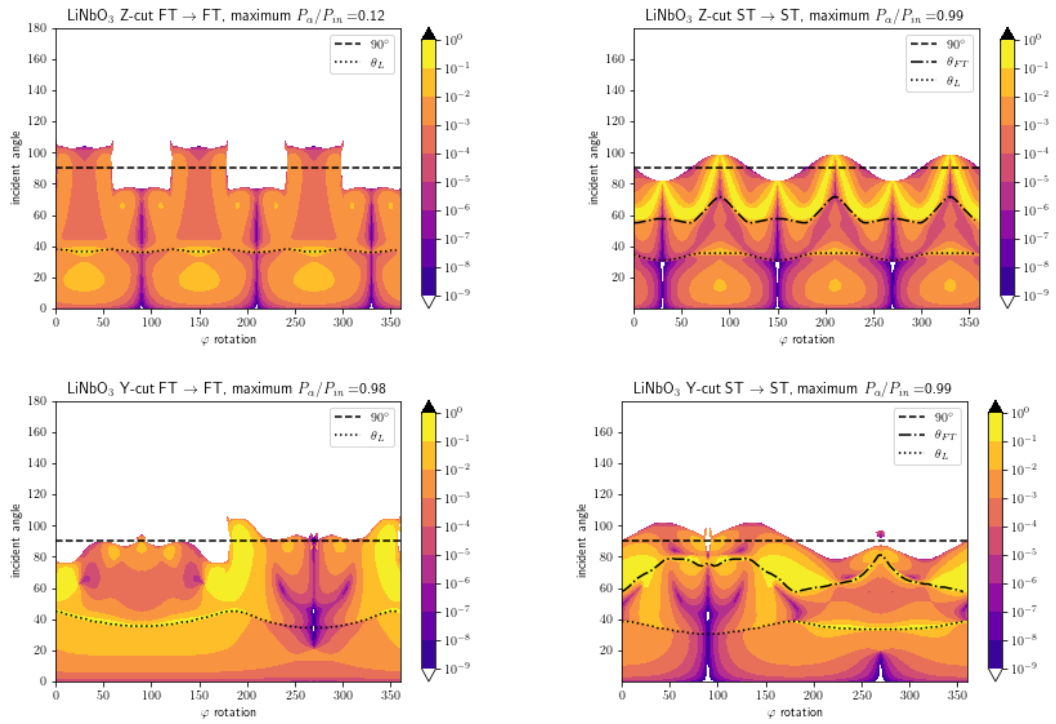

Figure 8. Highest power transmittance mode pairs on Z- and Y-cuts.

mode has the highest power transmittance when the transmitted partial wave mode matches the incident mode.

Z- and Y-cuts demonstrated power flow at incident angles beyond the 0° to 90° interval, see Fig. 8. This is due to the concave nature of the slowness surfaces and the relation of group velocity to the slowness surface. In concave parts, the group velocity's k_z component had an opposite sign to the phase velocity's k_z component, leading to energy flowing towards the opposite solid under lossless and sourceless medium assumptions.

Plots for X-cut were not included as the phase velocity labeling doesn't map one to one on quasitransverse modes. The slowness curves of FT and ST modes cross a total of four times, see Fig. 10. This means that with the phase velocity labeling convention, it would seem that both slow and fast transverse modes change polarizations in the four crossing points, while in reality one of the modes is a pure shear with polarization in X-axis direction, and the other is a quasitransverse mode. The pure shear is not piezoelectrically active because all displacements in X-axis directions are mirrored and therefore do not induce polarization of the solid. This can easily be seen by comparing slowness surfaces with and without the piezoelectric

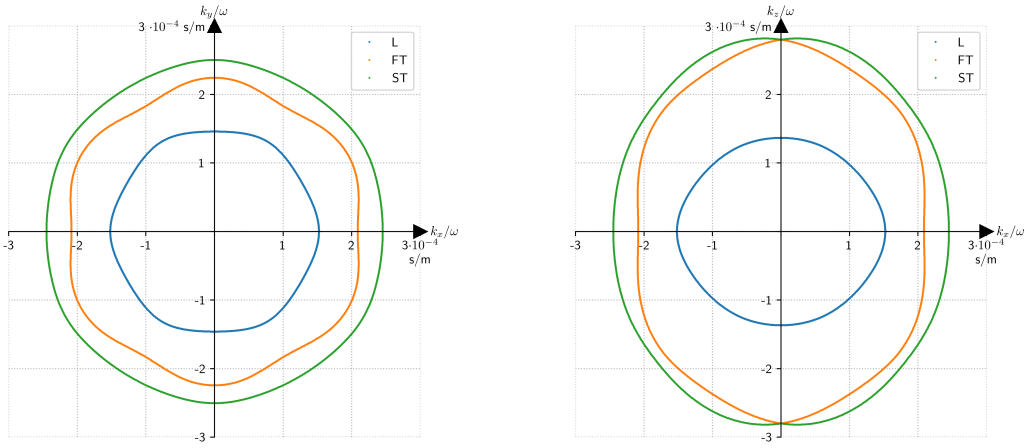

Figure 9. Slowness surfaces of $LiNbO_3$ Z- and Y-cuts from left to right. Plots were calculated with $\varphi = 0°$ rotation while taking the piezoelectric effect into account.

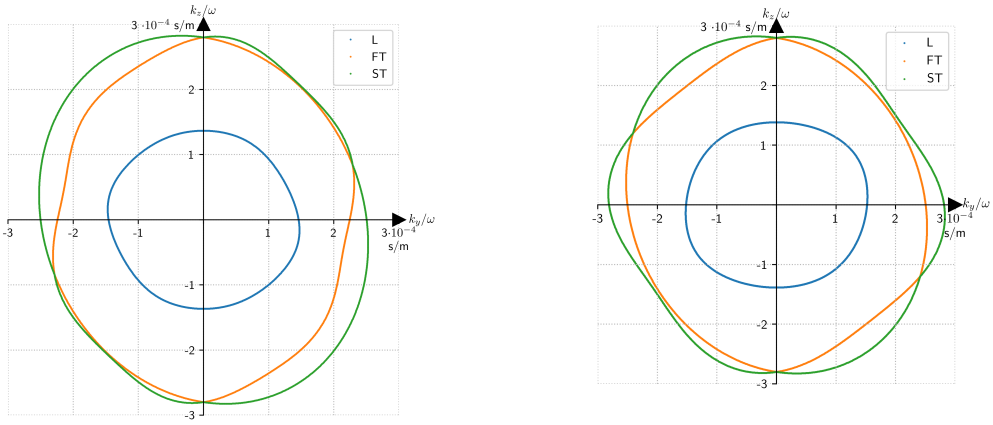

Figure 10. X-cut slowness surfaces with the piezoelectric effect on the left, and without it on the right.

crystal cut	Heat flux ($\mu W/m^2$)
Z	2.1
Y	5.0
X	5.2

Table 3. Heat flux of $LiNbO_3$ on three different crystal cuts. Gap distance is 200 nm and temperature is 0.1 K

effect. Ultimately, correction of the X-cut color plots was deemed not worth the effort, as X-cut is not a possible configuration for phonon tunneling measurements in Sec. 4.

Calculation of tunneling heat flux for all three cuts showed that X-cut exhibited the highest flux, followed by Y-cut and Z-cut, with parameters for gap width ($d = 200$ nm) and temperature ($T = 0.1$ K). The three fluxes can be found in Table 3. Y-cut heat flux is expectedly larger than Z-cut heat flux, as the dominant piezoelectric axis (Z-axis) is aligned with the vacuum gap surface, and can then excite even stronger electrical field from evanescent mode to enhance flux. This is seen also in X-cut, which exhibited an even stronger flux than the Y-cut due to both piezoelectric axes lying in the crystal plane. However, the increase was more modest in comparison, as the piezoelectric response was much weaker in the Y-direction.

Finally, we can estimate transmitted power from tunneling flux with an example radiator. The above heat flux is calculated based on the assumption of two semi-infinite half-spaces, but we can use these results to estimate the transmitted power for finite surface area. With flux of $5.0 \cdot 10^{-6}$ W/m^2 with Y-cut and an example radiator of 0.6 μm in height h and 50 μm in width w, the resulting power flow from phonon tunneling is $J^{\mathrm{PE}}wh = 1.5 \cdot 10^{-15}$ W, which can be demonstrated experimentally by measuring the temperature difference of two solids in steady-state [7]. Devices measuring transmitted power should be built to have tunneling either in Y-direction or X-direction to have a stronger transmitted power.

4 Investigation of fabrication methods

In order to study the piezoelectrically mediated acoustic phonon tunneling phenomenon in lithium niobate, sample fabrication was investigated on lithium-niobate-on-insulator silicon chips. The chips in use were from NanoLN company, with 600 nm of single crystal $LiNbO_3$, 4.5 µm of thermally grown SiO_2 and 500 µm $\langle 1\,0\,0 \rangle$ Si. The $LiNbO_3$ in use is X-cut, meaning the surface normal of $LiNbO_3$ is the crystallographic X-axis, see Fig. 11. Fabricated samples are suspended thin films of $LiNbO_3$, which are patterned into two suspended pads that are in close proximity to each other. Suspension is required to reduce the heat flow from the film to the substrate and to maximise the detection of tunneled heat flow. Four Superconductor-Insulator-Normal metal-Insulator-Superconductor-junctions (SINIS-junctions) are fabricated on top of the pads to function as thermometers and heaters, two for each pad, see Fig. 12.

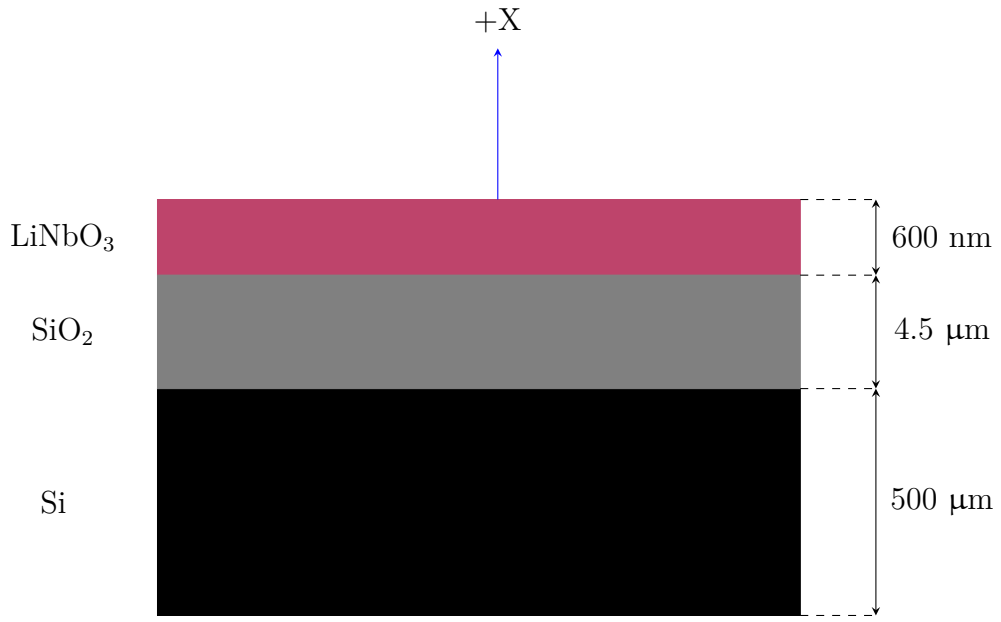

Figure 11. Illustration of the LNOI-chips used for research.

The general work flow of fabrication was to first pattern the $LiNbO_3$ layer, then to evaporate the gold wires and the Al-Al_2O_3-Ti-Au SINIS-junctions, and to finally

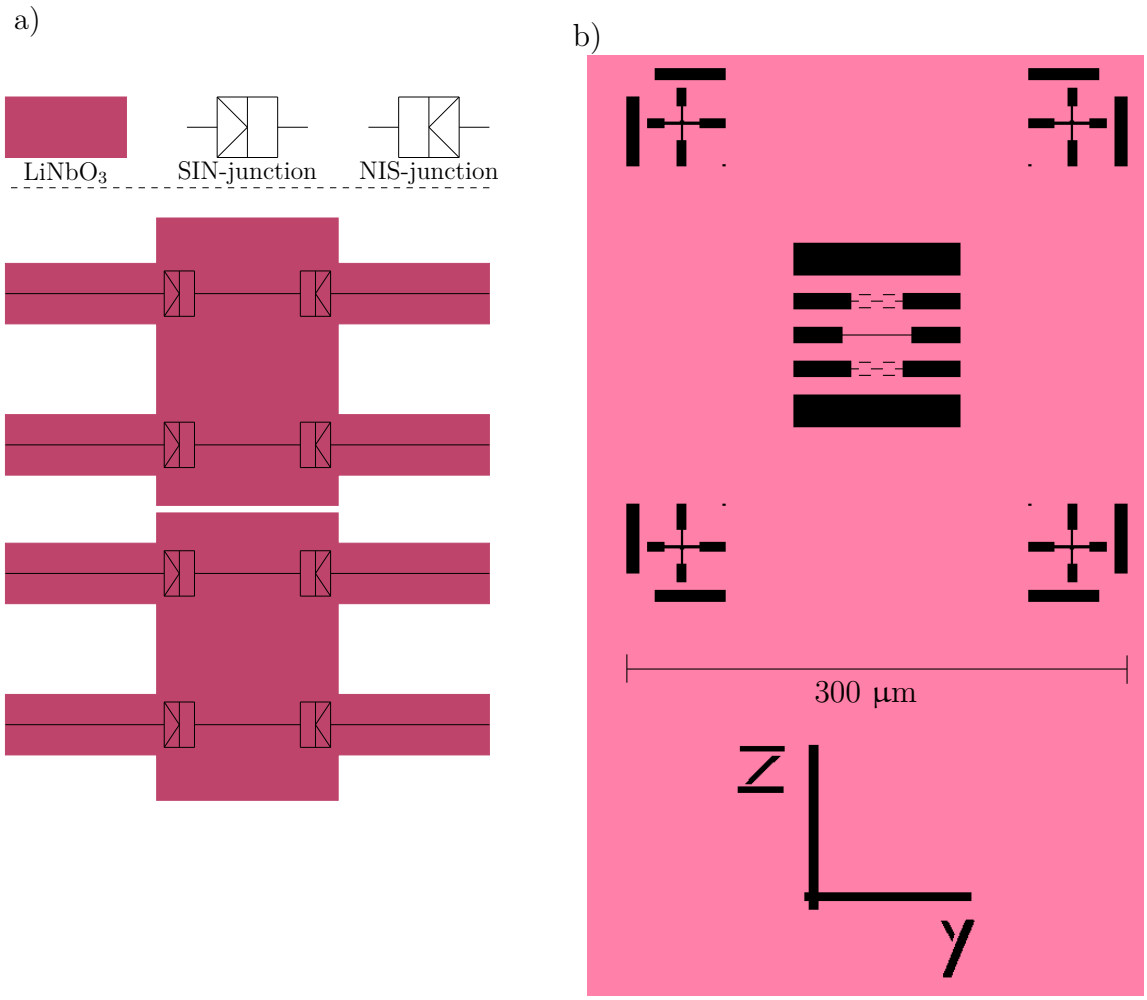

Figure 12. a) A diagram of the phonon tunneling sample with the SINIS-junctions as measurement devices with the first, simpler pad design. b) Illustration of the second EBL pattern for $LiNbO_3$ etch. Black areas signify exposure to positive tone resist, with the exception of the 300 µm measure. Four cross shapes in the corners are for the writefield alignment in metallization phase of the fabrication. Z and y at the bottom mark the crystallographic surface coordinates. In the middle the self supporting pads are visible. The slits in the self supporting pads are there to help with the HF vapor etching in the structure release step.

release the $LiNbO_3$ pads from SiO_2 with a HF vapor etch. A flow chart illustrating the process is shown in Fig. 13. Fabrication was done in the NSC cleanroom with the following equipment: Sonicator for cleaning chips, BALZERS electron gun evaporator for Cr and Al_2O_3 deposition, Laurell WS 650 Spin Coater for resist spinning, Raith eLine electron microscope for imaging and electron beam lithography, OXFORD RIE-CVD for plasma etching, an electron gun ultra-high vacuum (UHV) evaporator for Al, Ti and Au evaporation and Al oxidation, HF etcher for HF vapor etching and profilometer for etch depth measurements.

4.1 Preparation of LNOI-chips

Chips were prepared by spraying photosensitive lacquer from a spray can on the $LiNbO_3$ side and then sawing the wafer to 5 mm $\times$ 5 mm chips using a silicon saw. After dicing a quarter of the wafer, the diced chips were taken for experimental use, and the crystallographic Z-direction was marked on the backside of the quarter for future reference. When chips were cleaned for use, the Z-direction was scratched on the silicon side of each chip with the silicon scribe.

The chips were cleaned with boiling acetone and cotton tip scrubbing, followed by a sonication and a isopropanyl (IPA) rinse. After the cleaning, a hardmask was deposited with physical vapor deposition (PVD) using BALZERS electron gun evaporator. Chromium was selected as a hardmask to pattern $LiNbO_3$, as it is resistant to fluorine based plasma etches [24, 25, 26] and it was used in [26] as a hard dry etch mask for $LiNbO_3$ fluorine-argon gas recipe. A layer of 100 nm thick chromium was deposited on $LiNbO_3$ by BALZERS vacuum evaporator, and later the thickness was increased to a minimum of 150 nm thick mask due to $LiNbO_3$ dry etch recipe etching through the chromium mask. The thickness for the etch masks was measured with a profilometer as the thickness meter of the evaporator is unreliable even with a calibration.

4.2 $LiNbO_3$ etch mask

Both wet etching and dry etching of Cr were investigated as ways to transfer the patterns from e-beam resists. Wet etching was investigated for its ease of use, availability and speed, whereas dry etching is an anistropic technique and usually more suited for sub micron etches. The following subsections diverge after chromium evaporation but follow the same sample fabrication steps after chromium etch. Design

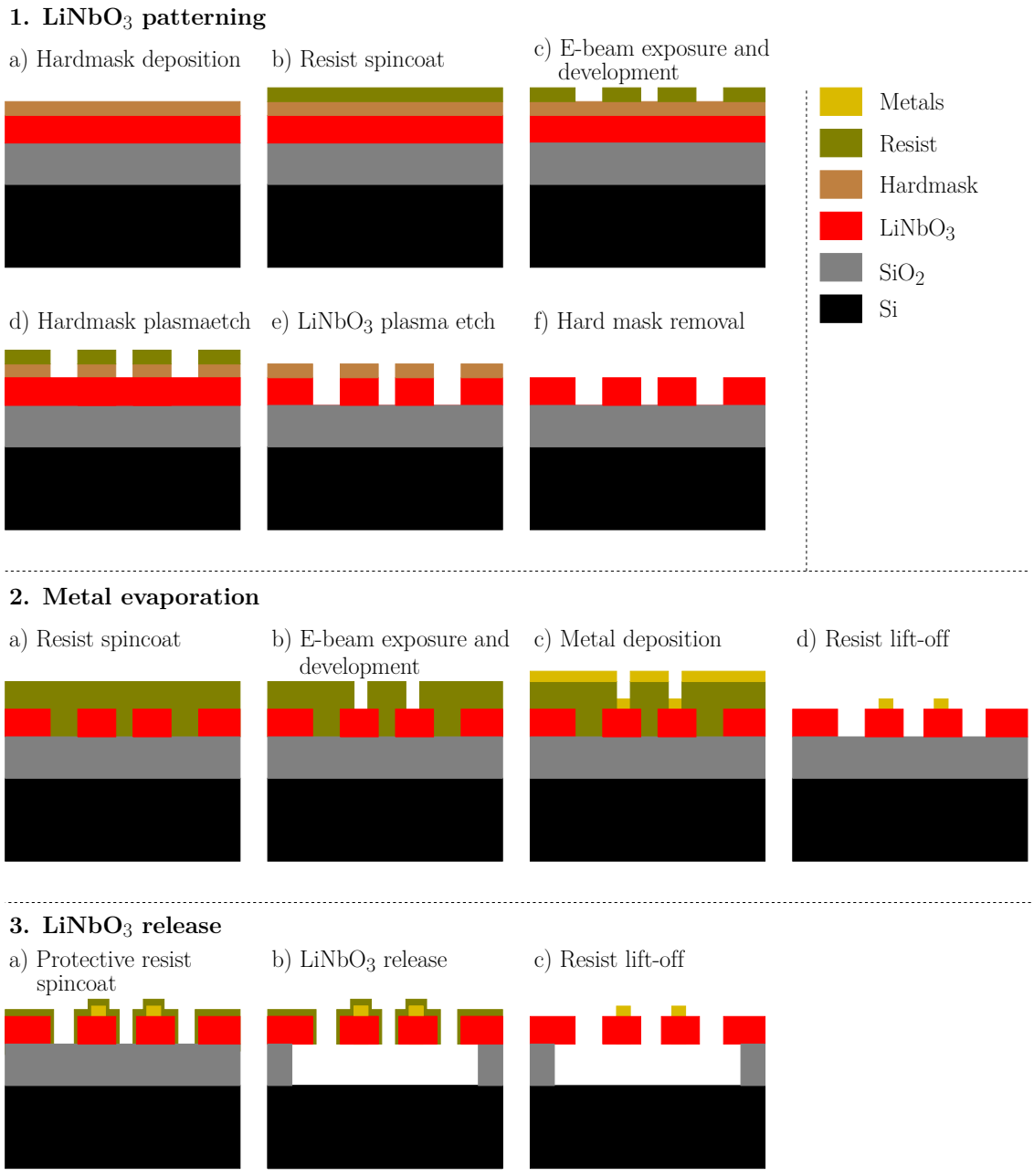

Figure 13. Step by step illustration of the general steps of sample fabrication.

for the $LiNbO_3$ etch pattern is illustrated in Fig. 12.

4.2.1 Cr wet etch

The wet etch mask for chromium etching was fabricated from poly(methyl methacrylate) 950 000 in molecular weight diluted to 4% by weight in anisole, commonly abbreviated as PMMA 950k A4. The resist was spun on SPINNER 2500 RPM for 1 minute and baking it on a hotplate in 160 °C for 3 minutes, leaving a 300 nm thick PMMA layer.

PMMA layer was patterned with Raith eLine SEM (Scanning Electron Microscope) using EBL (Electron Beam Lithography) to weaken crosslinking in the PMMA polymer. Weakened areas were removed with a developer of 2:1 isopropanyl:methyl isobutyl ketone solution (Dev 1) revealing the pattern drawn with EBL. The chromium patterns for suspended structures include larger openings for the definition of pads, and a precise and narrow gap for phonon tunneling. The e-beam software had two sets of parameters for the electron beam, one for the narrow gap and one for the other structures. For all structures an accelaration voltage of 20 kV and a dose of 250 $\mu C/cm^2$ were used. Larger structures were patterned with a 200 µm writefield and with a 120 µm aperture, and the tunneling gap was patterned with a 100 µm writefield and a 30 µm aperture.

At first, chromium was etched with a commercial Aldrich NiCr wet etch, which is based on a mixture of ceric ammonium nitrate and nitric acid. The etchant etched larger areas too fast, at most taking 2 minutes to etch 100 - 200 nm of chromium, while having harder time penetrating the narrow sub micron gap to etch the tunneling gap. As the commercial NiCr etch was too unreliable for good sample yields, 5 : 9 : 40 by weight NaOH : $K_3[Fe(CN)_6]$: H_2O chromium etch solution was investigated for a possible wet etch. The recipe for the chromium etch is a mixture of 1 part 50 g of NaOH diluted in 100 g of H_2O and 3 parts of 30 g $K_3[Fe(CN)_6]$ diluted in 100 g of H_2O. For this etchant, the differences between the gap and the larger areas were less, and its etch speed was slower than NiCr etch. The slower etch speed allowed for increased control of the etch, and thus increased sample yields. Also the chromium etch seemed to produce smoother edges. Fig. 14 shows an example of Cr wet etch result for an initial 50 nm gap in etch mask.

In the end, wet etching chromium wasn't a good method to pattern chromium. Wet etching with either etchant was too uncontrollable, which lead to worse sample

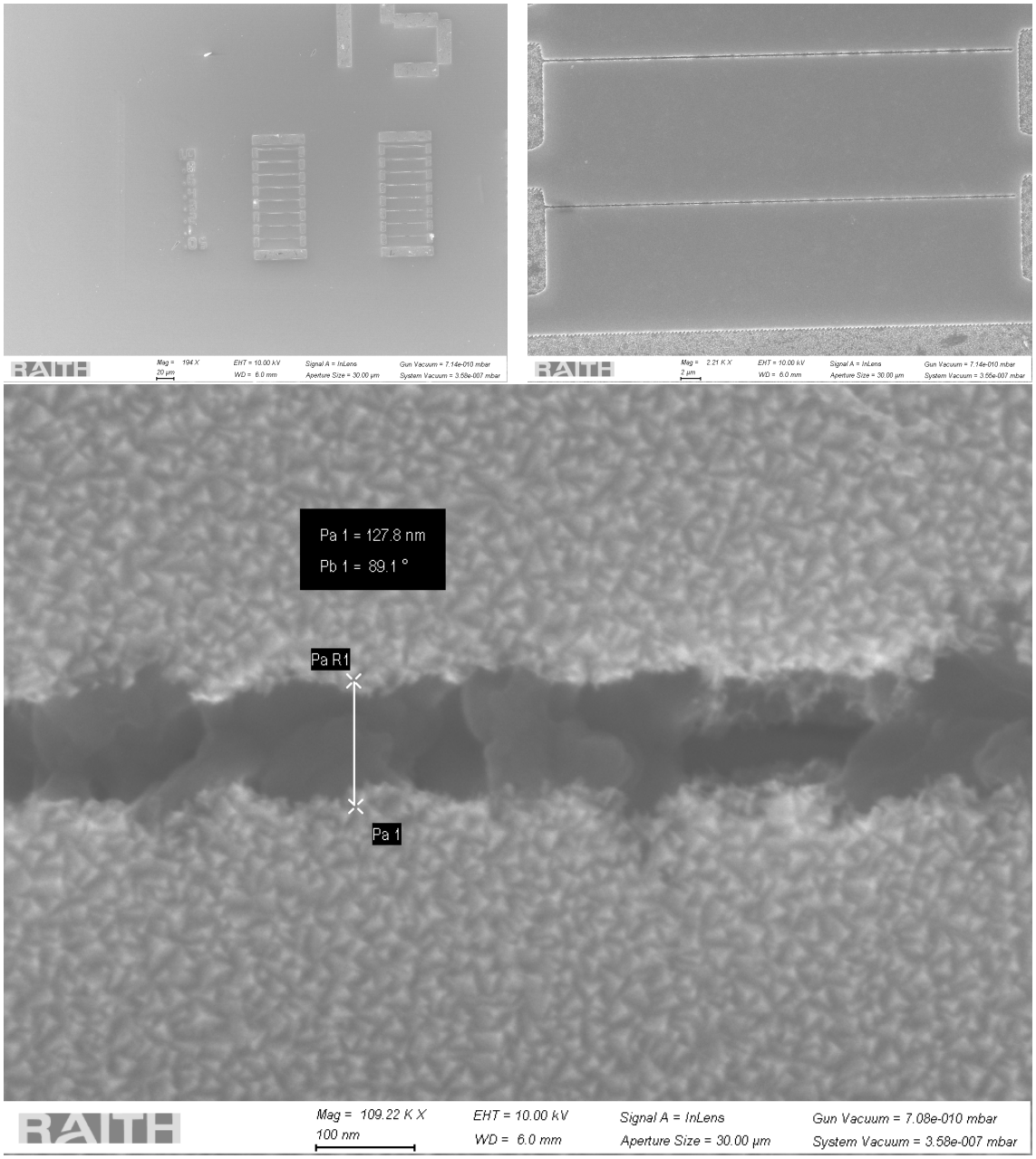

Figure 14. Chromium layer of 250 nm thick etched with 5 : 9 : 40 $NaOH:K_3[Fe(CN)_6]:H_2O$ solution for 2 minutes in room temperature. Sample was shaken in the solution for 10 seconds at the start of etch. After etch sample was passivated in de-ionized water and rinsed in IPA and then blow dried with nitrogen. Highlighted gap is a 50 nm nanometer gap in SEM software that has widened to 130 nm mostly due to isotropic nature of wet etch. Tightest gap of 50 nm is also only partly etched.

yields. In addition the gap edge quality is rather rough, which together with all the other problems listed in this Section prompted us to investigate dry etching methods of Cr.

4.2.2 Cr dry etch

Because the pattern transfer for a smooth tunneling edge was too hard to achieve with a wet etch step, a two-step dry etched pattern transfer process for the Cr was investigated. The dry etch process involved depositing a layer of chromium, a layer of Al_2O_3 and a layer of mr-PosEBR 0.3 as the e-beam resist. Both chromium and Al_2O_3 were deposited with the BALZERS electron gun evaporator.

Evaporated Al_2O_3 was chosen as a hard chromium etch mask for its general durability and ease of deposition with chromium, as it could be deposited in the same evaporation run as chromium. Layer of Al_2O_3 or similar material is necessary as an intermediate mask because the Cr plasma etch recipe is a high power oxygen plasma, which is used for ashing most e-beam resists. In practice evaporations, the two were done in separate sessions to measure the thickness of chromium layer, as the evaporator was too unreliable to achieve similar consistent thicknesses.

Al_2O_3 was patterned with a positive tone e-beam resist. Mr-PosEBR 0.3 was spun on top Al_2O_3 to pattern Al_2O_3 as the Cr etch mask, because of its reportedly high resolution and better etch durability[27]. A single layer of mr-PosEBR 0.3 was spun with 3000 rpm for 1 min and then baked at 160 °C for 1 min, which resulted in 300 nm layer of resist. A double layer resist of mr-PosEBR 0.3 was also investigated for the possibility of thicker hardmasks. The parameters for a double layer resist were the same as in the single layer for both layers, which resulted in around 500 nm layer of resist.

The evaporation thicknesses for single layer resist were around 150 nm for Cr and 30 nm for Al_2O_3. Double layer resist allowed for thicker hardmasks in the etching sequence, which then allowed the Cr layers to be around 180 nm and the Al_2O_3 at least 50 nm.

Mr-PosEBR 0.3 was patterned with SEM with the same parameters as PMMA in Sec. 4.2.1, with the notable exception being a much lower dose, as mr-PosEBR 0.3 is much more sensitive to electron radiation. The development was done with mr-Dev 800 commercial developer for 1 minute, followed by 1 minute of passivation in IPA.

Next, Al_2O_3 was dry etched with 10 sccm of SF_6, 40 sccm of Ar, 20 mTorr

chamber pressure, 250 W RF-power and 10 °C with a helium backing to cool and stabilize the sample stage to sub room temperature. The recipe was a pre-installed recipe in the Oxford RIE. Use of the machine recipe was motivated from earlier etch mask tests on Al_2O_3 using $LiNbO_3$ etch recipe, which is very similar to the pre-installed recipe. The recipe is also in line with findings from Ref. [28], as it was a low pressure, high power SF_6/Ar recipe. Etch rate according to the recipe was 18 nm/min. The etch speed for mr-PosEBR 0.3 was calculated to be around 120 nm/min from profilometer depth measurements. Selectivity of Al_2O_3 to mr-PosEBR 0.3 is 1:6.7.

Taking inspiration from [25], chromium was dry etched with an unusual oxygen plasma based recipe. The etch rate is strongly dependent on the relative gas flow of SF_6 to O_2, and it has a sharp peak with just trace amounts SF_6 mixed with O_2 flow, at around 0.75 %. The etch recipe used was 100 sccm O_2, 2 sccm SF_6, 300 W RF power, 100 mTorr chamber pressure and 40 °C table temperature. Recipe is not the same as in [25] due to machine limitation on maximum oxygen flow and minimum SF_6. As the recipe is oxygen plasma based, Al_2O_3 was used as a hardmask for the Cr etch. Etch speed was determined to be around 60 nm/min to 70 nm/min, which was calculated from etch depth measured by profilometer. The etch speed of Al_2O_3 calculated from profilometer depth measurements was surprisingly high, around 5 nm/min to 15 nm/min. Selectivity of Cr to Al_2O_3 ranges from 4:1 to 14:1, though from experience it is much closer to 4:1 than 14:1, which further investigation needs to verify.

The two-step dry pattern transfer from the resist to $LiNbO_3$ has a lot of advantages over wet etching. The biggest advantage is the improved capability to make smoother edges, which are expected to be critical in tunneling gap measurements to compare to the currently established theory. The second advantage is that the etching behavior is more uniform over different scales of openings, while the wet etching has trouble penetrating tight gaps to etch properly. The third advantage is that dry etching is more reproducable after process parameters have been properly defined.

4.3 $LiNbO_3$ dry etch

Etching of $LiNbO_3$ proved to be somewhat challenging with the given conditions. Etching recipes were investigated for the older Oxford RIE plasma etcher unit due to concerns over contaminating the newer ICP-RIE unit with LiF compounds. These LiF compounds could, in theory, micromask other samples with rather etch resistant material and ruin etch recipes. Also etch recipes in the literature for X-cut $LiNbO_3$ with a conventional RIE-unit were few, but most promising recipes for RIE and ICP-RIE were usually with a mixture of Ar and SF_6 gasses. Some recipes found included: Z-cut etch with 1:1 flow ratio of Ar and SF_6 using a ICP-RIE unit [29] or with $Ar/CF_4/H_2$ mixture using a conventional RIE [30, 31], X-cut etch with Ar and a ICP-RIE unit [32, 33] or a with SF_6 gas using a conventional RIE [34].

A fairly well working etch recipe was found to be a mixture of Ar and SF_6 gases both with flow of 10 sccm, 50 mTorr of chamber pressure, 200 W of RF-power, 30 °C using a chromium hardmask with an etch time of 100 minutes. The approximate etch rates were measured to be $6 - 8$ nm/min for $LiNbO_3$ and $1.5 - 1.8$ nm/min for Cr, measured after each etch with a profilometer. The selectivity of $LiNbO_3$ to Cr at its worst is then $3.33 : 1$, which is adequate considering how hard to etch $LiNbO_3$ is. Higher power recipe of 300 W allowed for shorter etches of 60 minutes. However, the high power etches were more prone to burn through the etch mask and roughening the $LiNbO_3$ film surface, reducing sample yields in the metallization step. This was due to tighter error margins. Lastly, with the high power etch it was harder to maintain a stable sample stage temperature compared to the lower power recipe.

Compared to the plain argon recipes used with an ICP-RIE unit [33, 32] the used recipe sacrifices sidewall angle for the ability to use positive tone pattern transfering with the e-beams. The sidewall length from top view was roughly measured to be around $350 - 400$ nm, which means that the sidewalls are slanted at an angle of around $60° - 57°$, see Fig 15. For comparison, an angle of 90° would be a straight wall.

The edge quality of the etch is highly dependent on the quality of the etch mask edges, which in turn is more complicated as the pattern transfer has to pass three layers (resist-Al_2O_3-Cr) of etch masks instead of just one or two layers. However comparing the results from the three-step dry etch in Fig. 15 to the results from the wet etched Cr in Fig. 16, there was a significant improvement in edge quality

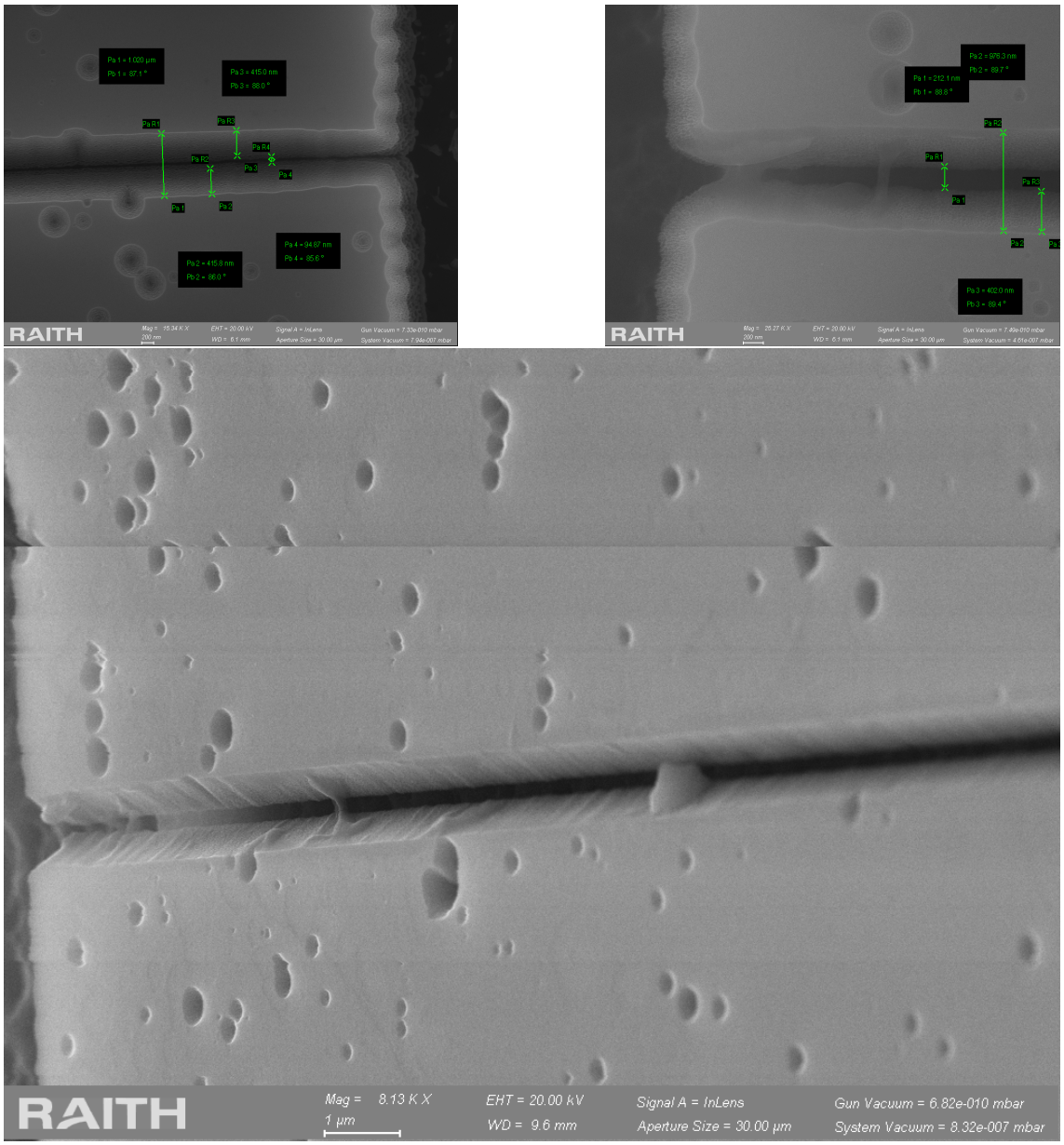

Figure 15. $LiNbO_3$ patterned with a three-step dry etch process. The upper left picture is right after the dry etching, and the upper right and the bottom pictures are after HF vapor release step. Results highlight the improvement in edge quality over the wet etching technique. Sidewalls were measured to be 400 nm long from the top view after the HF vapor etch and the gap was measured to be 200 nm wide. Before the HF etch it can be hard to identify $LiNbO_3$ edges from SiO_2, and generally visual measurements from SEM images tended to somewhat overestimate the sidewall length and underestimate the gap size. The craters on the surface of $LiNbO_3$ are from $LiNbO_3$ dry etch burning through the etch mask. The dirt on the tunneling gaps are from an unconfirmed source, but it is suspected to be partly from redeposition products in $LiNbO_3$ dry etch and partly from insufficient cleaning.

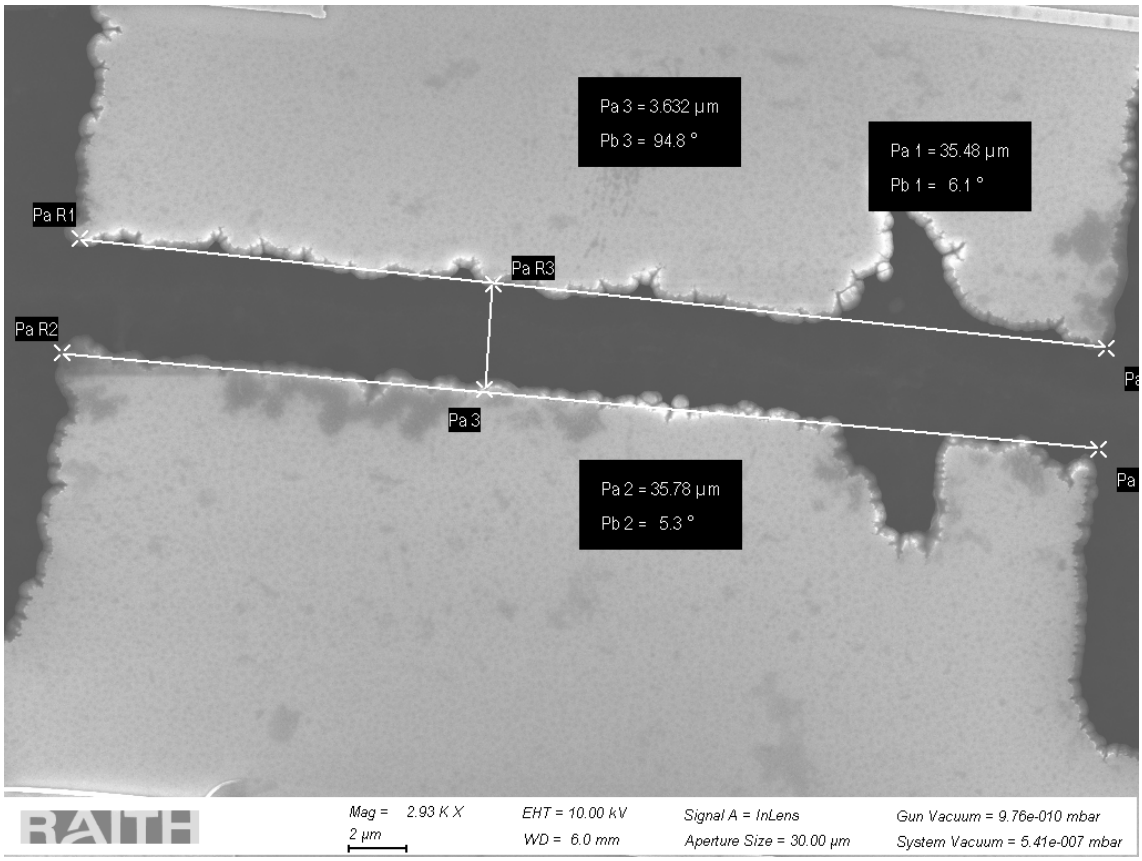

Figure 16. $LiNbO_3$ patterned with wet etched chromium mask and a SF_6/Ar dry etch process. Patterned platforms were released from SiO_2 with a HF vapor etch. A big gap size of over three microns and jagged edges are a result of patterning chromium with the wet etching recipe.

over the wet etching step with the three-step dry etch process, without any major optimizations.

4.4 Metallization

The second round of fabrication was done on the defined structures to set up sensors and heaters on the sample to be able to detect phonon tunneling. After the $LiNbO_3$ dry etch step, chips were cleaned in hot acetone, sonicated, rinsed in IPA and blow dried with N_2. Then the chips were first spin coated with 9% ethyl lactate (EL-9) 2500 RPM for 1 minute and baked in 160 °C for 1 minute, which results in 350 nm thick resist layer. A second layer of EL-9 was spun and baked with the same parameters, totaling the EL-9 layer to 700 nm. PMMA 950k A4 was then spun on top with 2500 RPM for 1 min and baked in 160 °C for 1 minute as a third layer.

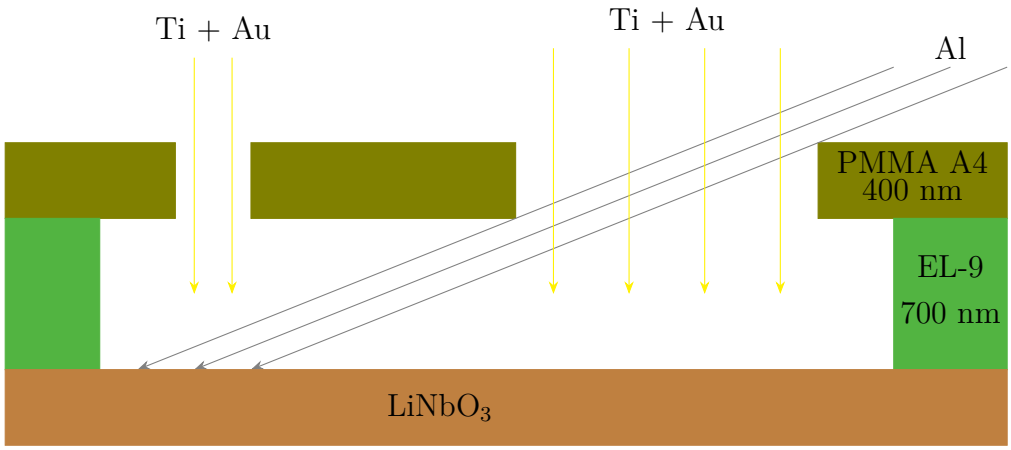

Figure 17. Illustration of the shadow evaporation technique used in the SINIS-junction fabrication. First Al is evaporated at an angle and following that Ti and then Au are evaporated from a right angle. The opening on the left is where the Al-Al_2O_3-Ti-Au junction is formed. Au-line that forms on the right is a byproduct of the technique and is not of any importance.

A fourth layer of PMMA was spun and baked with same parameters to achieve approximately a 500 nm thick PMMA layer.

A combination of EL-9 and PMMA A4 is used because EL-9 is more sensitive to direct e-beam exposure than PMMA, as well as the backscattered electrons, and the exposure area is thus much larger than PMMA with the same beam parameters. This double layer resist results in a smaller opening in the PMMA layer and a larger cavity in the EL-9 layer underneath the PMMA layer. The cavities can be utilised in a shadow evaporation technique, in which the evaporated metal can be blocked access to narrower openings by the top layer PMMA at large evaporation angles. An illustration of the technique is shown in Fig. 17.

The e-beam exposure of the double layer resist can be more challenging than the exposure of the $LiNbO_3$ pad patterns. High precision is required in focusing, stitching for the longer metallizations, and alignement to have working samples, so extra care is needed on the patterning. The parameters for the e-beam are similar to the ones described in Sec 4.2.1, when bonding pads and metal wires from pads to junctions were patterned with a high current of 4.9 nA, an aperture of 120 µm and a maximum writefield of 1000 µm (see Fig. 18). The SINIS-juntions were patterned with a 0.32 nA current, a 30 µm aperture and a 200 µm writefield. Both high and low current settings had a 20 kV accelaration voltage and a 250 $\mu C/cm^2$ area dose.

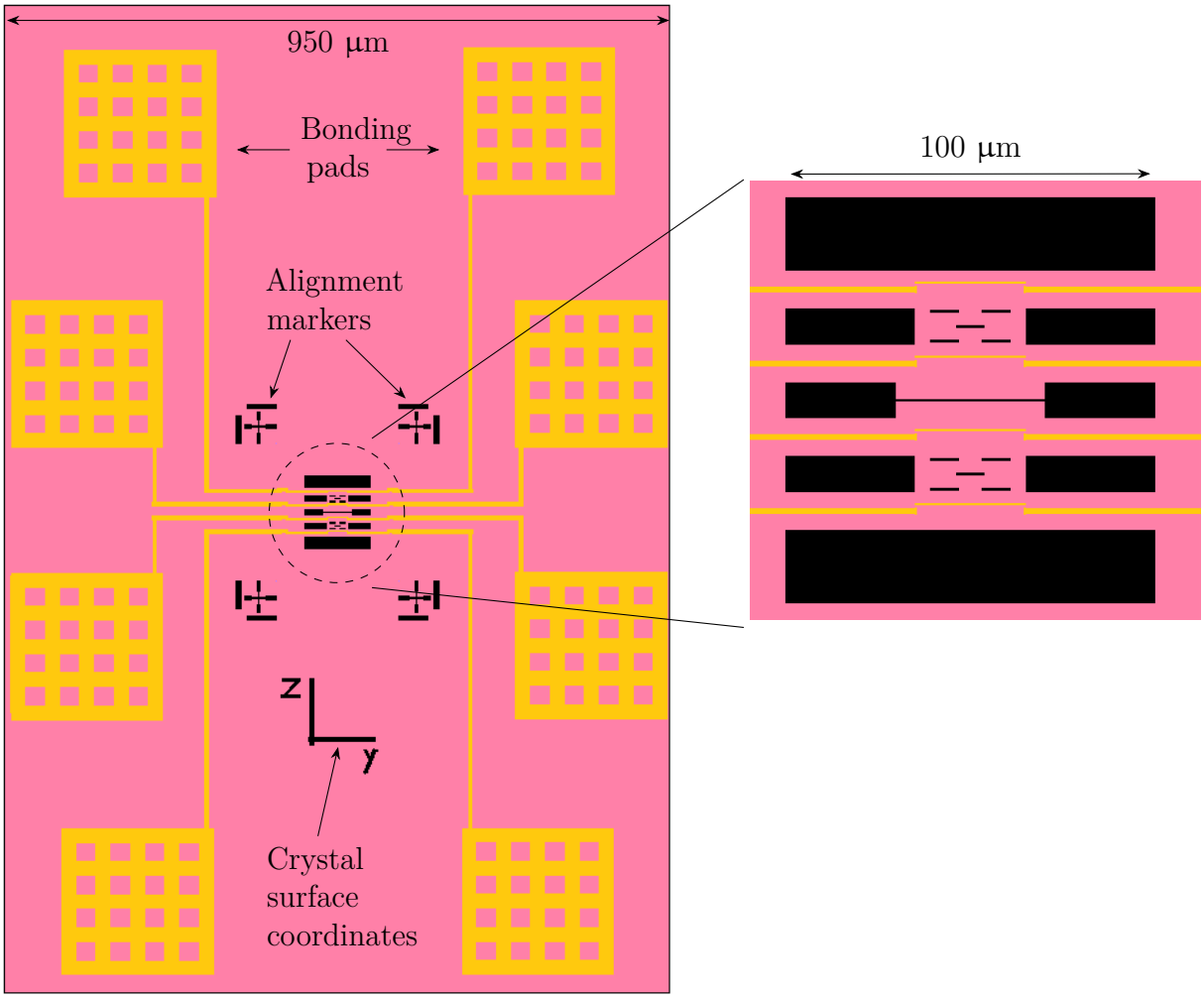

Figure 18. Full design of the phonon tunneling sample with a second pad design. SEM exposure areas of metallic parts such as the bonding pads, the wires and the SINIS-junctions are in yellow, the pink backround is the $LiNbO_3$ surface and the black signifies areas that have been etched in the earlier lithography phase. The slits between the SINIS-junctions on each platform are there to let the HF vapor through the middle of the platform for shorter etches.

Design for SINIS-junctions and bonding pads can be found in Fig. 18.

The development of the patterns was a two-step process, because EL and PMMA have different developers. First, the PMMA A4 layer was developed with 40 s in Dev 1 (2:1 IPA:MIBK) and then EL-9 layer under was developed in Dev 2 (2:1 Methanol:Methoxyethanol) for 9 s. After the development, the sample was submerged in IPA for a minute for passivation and to clean any dirt.

Before the metal evaporation, samples were treated quickly with an oxygen plasma in RIE to remove any resist residue, enhancing the yield of working SINIS-junctions. The recipe for the O_2 cleaning etch was with 60 W RF power, 40 mTorr pressure, and 50 sccm flow of O_2 for 30 s. The junctions were then evaporated with the ultra high vacuum electron gun evaporator (UHV), first starting with the evaporation of Al at an 70° angle from the surface normal. Al was evaporated with a speed of 0.1 nm/s for 55 nm in the thickness meter, which corresponds to 20 nm thin film. After the Al evaporation, samples were taken back to the load lock for oxidation without breaking vacuum. Oxidation was done for in pure oxygen in 200 mbar for 5 min. Then Ti was evaporated on the sample at 0° angle for 4 nm at a speed of 0.1 nm/s, after which Au was evaporated on top of Ti also at 0° angle for 40 nm at a speed of 0.1 nm/s.

The evaporations were followed with resist lift-off. Chips were immersed in hot (50°C) acetone and sprayed with hot acetone using syringes while submerged. This helped to peel off the metal coated resist layer, and to clean smaller corners between electrode lines that would usually stay stuck without turbulence induced by the syringe treatment.

Junctions were tested with a volt meter using indium tips to probe the junction bonding pads. Junction resistance values over 3 kΩ indicated a possibly working SINIS-junction.

4.5 Tunneling structure release

The main method for releasing $LiNbO_3$ layer from SiO_2 layer was HF vapor etching. Vapor etching was chosen because of the challenges of the conventional KOH Si etching method. Because of the LNOI-wafer structure, a backside KOH etch mask would be needed to be grown and patterned on Si, which would also require ashing and cleaning of the backside from an unknown substance. Also in addition to the Si etch, the SiO_2 would need to be etched from the backside as well, to realise a

free $LiNbO_3$ membrane. A free $LiNbO_3$ membrane only adds more problems to fabrication because doing either $LiNbO_3$ patterning or SINIS-junction fabrication first complicates the other. In contrast, the final vapor etching step only needs a protective layer on top of the metals which is a better starting point for the structure release.

HF vapor etch rate of SiO_2 at stage temperature of 35 °C was estimated to be around 0.5 µm/min, by roughly measuring undercut length in the lateral directions with SEM imaging, see Fig. 19. Samples could be etched in room temperature with the stage heater turned off with an estimated etch rate of 2 µm/min. This is expected behaviour, as higher stage temperatures reduce the amount of condensed water available for HF[35], which in turn reduce etch speed. However, etching in room temperature collects water underneath $LiNbO_3$ surfaces, which introduces the same stiction problems that the conventional HF wet etch has. If etch time is an issue, it is then recommended to just use the conventional HF wet etching over the HF vapor etching, which is significantly faster than the HF vapor etching [24]. The main advantage of the HF vapor etching is to avoid the stiction problems alltogether by sacrificing etch speed.

Etching without any protective layer on electrical components leads to visibly roughened gold layers, and in general it reduces the adhesion of the evaporated metals, so much so that the metals can peel off while trying to measure junction resistance with the indium tips. This leads to the inability to measure resistance of the junctions, and therefore the lack of capability to verify if the junctions are still working.

Al_2O_3 was tested as a protective layer [36, 37]. In principle the evaporation of Al_2O_3 should have been able to coat electrical components without blocking the HF vapor acces to SiO_2, as the trenches in SiO_2 layer from $LiNbO_3$ dry etch were in µm range. Al_2O_3 was evaporated on top of sample with varying angles on the same evaporation using BALZERS and different thicknesses of $Al_2O_3$was tested. Thicknesses in tens of nanometers didn't protect electrical components from corrosion and thicknesses in 100 nm - 200 nm range were too thick to measure resistance over the junctions.

Corrosion of the SINIS-junctions in the very final steps of fabrication proved be too challenging to solve in the timeframe allotted to work on the thesis. Therefore experimental work ends here, in the release step of fabrication. No measurements

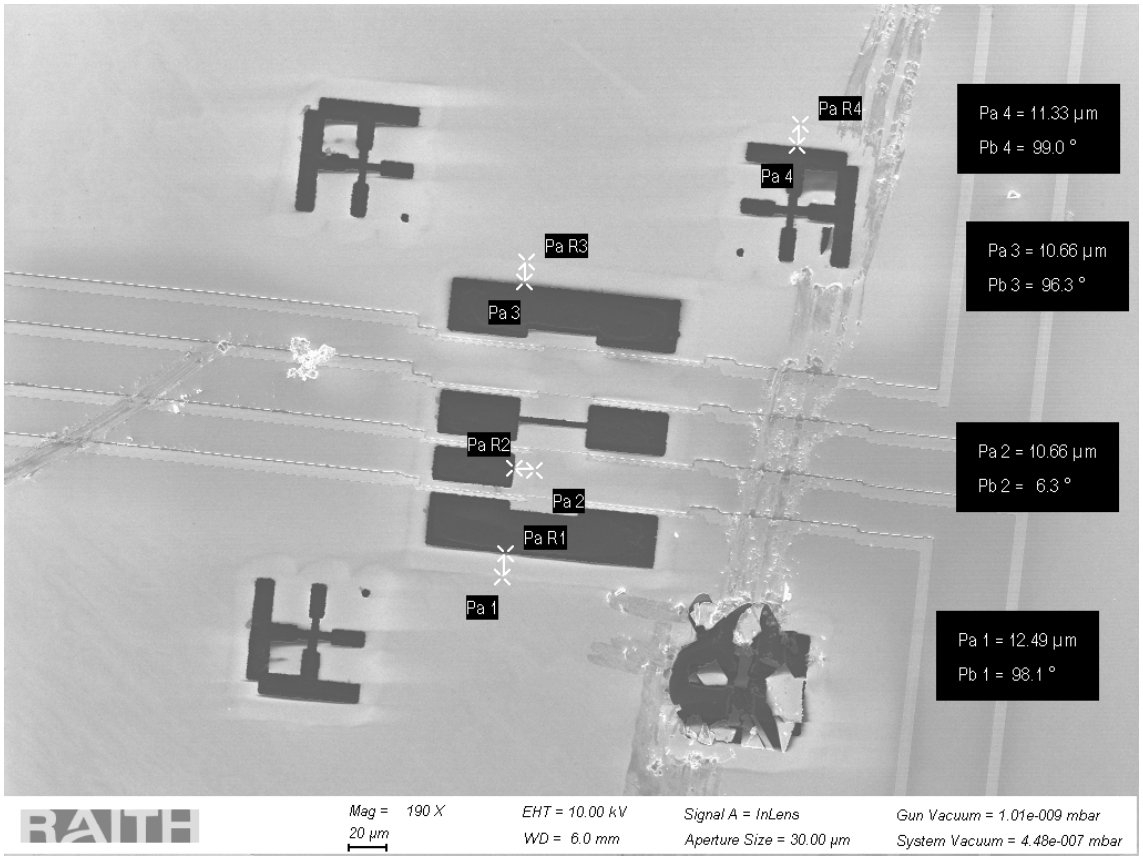

Figure 19. A SEM image of visual measuremetns of the HF vapor etch undercuts. The sample was etched for 20 minutes at 35 °C stage temperature, which resulted in a minimum of 0.5 µm/min etch rate.

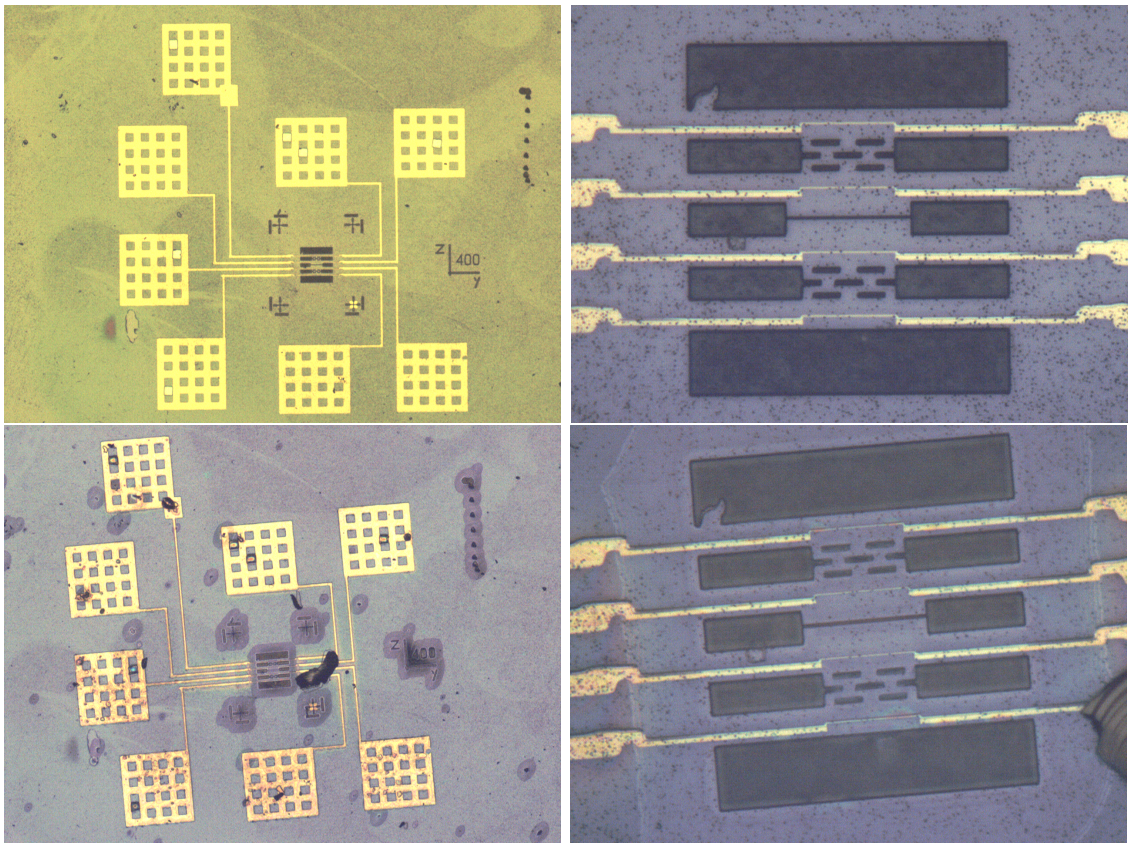

Figure 20. Pictures taken with the optical microscope before the HF vapor etch in the upper panels and after in the lower panels. All pictures are from the same sample and the pictures on the right are close up shots of the $LiNbO_3$ pads. On the lower left panel the darker circles around $LiNbO_3$ dry etches are from HF vapor etch undercuts.

could be made with broken or unfinished samples.

4.6 Fabrication results

Here are the results of sample fabrication. The main fabrication results concern patterning of the X-cut $LiNbO_3$ and HF vapor etch step.

Wet chemical etching turned out to be a poor technique to pattern Cr as mask for $LiNbO_3$. The edge quality of the wet etch was too rough to be used for the tunneling gap etches, as the roughness in Cr gap edge would later be transfered to $LiNbO_3$ through the dry etch. Wet etching also couldn't uniformly etch narrow gaps and large areas, which resulted in worse sample yields.

Dry etching of Cr was more reliable compared to wet etching techniques. Despite involving an extra lithography step of dry etching Al_2O_3 for Cr etch, the patterning

Mask	mr-PosEBR 0.3	Al_2O_3	Cr
Target	Al_2O_3	Cr	$LiNbO_3$
Gas flow (sccm)			
Ar	40		10
SF_6	10	2	10
O_2		100	
p (mTorr)	20	100	50
P (W)	250	300	200
T (°C)	10	40	30
Etch rate (nm/min)			
Mask	120	15	1.8
Target	18	60	6
Selectivity	6.7	0.25	0.3

Table 4. Dry etch recipes used to pattern LN in sequence. Maximum estimated etch rates for masks and minimum estimated etch rates are presented from earlier sections for mininum selectivity. Mask to target selectivity is used here.

results were both more reproducible and had better edge quality. The recipe is highly dependent on the e-beam resist used. Currently, thickness constraints of mr-PosEBR 0.3 bottleneck the recipe as a 300 nm thick resist layer can only cover the first 44 nm of Al_2O_3 etch, which in turn only covers 176 nm of Cr, which is just a few nanometers short of 180 nm that barely covers 600 nm of $LiNbO_3$ etch. Values were calculated using the minimum selectivities in Table 4. It is critical not to burn through the Cr layer and etch $LiNbO_3$ as the damaged surface of $LiNbO_3$ will reduce SINS-junction yields. Thicker resist layers were not an option as multiple layers of mr-PosEBR had worse edge quality with initial dose tests. Other e-beam resists need to be investigated for possible improvements on the recipe.

Finding a working dry etch recipe for $LiNbO_3$ proved to be easier than initially thought. Chromium performed well as a mask despite its rare use in literature [34, 38]. The addition of Ar flow, higher pressure and lower power allowed for better Cr to $LiNbO_3$ selectivity of 0.3 compared to 0.56 from [34], which was a trade-off for a lower $LiNbO_3$ etch rate of 6 nm/min compared to 16 nm/min [34] and less vertical sidewalls of 56°compared to 75°[34].

A minimum gap width of around 200 nm was achieved with the three-step dry etch recipe presented in Table 4. This was achieved from an initial 500 nm gap width on the SEM program. The gap sidewalls were slanted due to the redoposition of

material during etching and resulted in an estimated slant of 56° in sidewalls. The gap width was not entirely uniform as the corners of the platform were of slightly smaller gap size. A 100 nm gap could be achieved by reducing initial length in SEM program to 400 nm, but due to the corners of tunneling gaps tending to have smaller gap size sample yields may suffer.

The fabrication of free-standing $LiNbO_3$ membranes on LNOI-chips was successful with a HF vapor etch. The thermal SiO_2 etch rate was estimated to be 0.5 µm/min with vapor etching at 35 °C stage temperature and 2 µm/min while the stage heating was off and samples were at room temperature. Room temperature etches collected water underneath the platforms which caused stiction issues. There were no stiction issues with the slower etch, so it is recommended for use. HF vapor etch rates were unusually high compared to 60 nm/min [24] at room temperature or 15 nm/min [35] with stage at 35 °C, which in the case of fabrication was favorable, but it is still puzzling that the etch rates do not match values in the literature.

In the end, measurements of phonon tunneling could not be made because SINIS-junctions were expectedly incompatible with the HF vapor etch. HF is capable of damaging all the metals (Al, Ti, Au) used in the junctions [24]. Evaporated Al_2O_3 failed as a protective layer as either it didn't prevent corrosion with thicknesses under 100 nm or was too thick with thickesses over 100 nm to confirm if it actually protected SINIS-junctions from corrosion. How the HF vapor damages the junctions is currently unknown, as the Al_2O_3 layers were undamaged and junctions protected by them looked unaffected with an optical microscope, yet the junctions were consistently broken after the HF vapor step. For successful samples, the problem needs to be fixed using another protective layer, or completely avoided by rearranging the HF vapor etch step before the junctions are fabricated, or finding a way to use KOH-etching for membrane release.

5 Conclusions

In this work, lithography steps to fabricate self-supporting $LiNbO_3$ membranes from lithium-niobate-on-insulator silicon chips were demonstrated. Self-supporting structures were fabricated with cryogenic measurement of piezoelectrically mediated acoustic phonon tunneling in mind. Measurement of the phenomenon has already been done with AlN in our research group [7]. Measurements planned to be done on $LiNbO_3$ were to confirm predictions of a hundredfold increase in tunneling flux over AlN. However, measurements were mainly an end goal for laying the ground work of lithography techniques on $LiNbO_3$, on which this work presents good results.

Etching of $LiNbO_3$ turned out to be the least challenging aspect of fabrication. In the end, most of the dry etching recipes found in the literature used high power - low pressure argon in some form or another in all cuts and achieved. What seemed daunting at first was the mixed knowledge and lack of information about how the etch rate depends on different cuts. This was especially true as most of the recent research done on $LiNbO_3$ is much more focused on Z-cut fabrication with ICP-RIE, and it was hard to grasp if those recipes would even work on X-cut and a conventional RIE instead of ICP-RIE.

The three-layer etch mask of mr-PosEBR - Al_2O_3 - Cr showed promising results in edge quality and etch resistivity. Cr is very suitable for etches that usually have poor selectivity when the etch recipe is more based on the physical aspects of ion bombardment. This three-layer mask could be used for other etch recipes, especially with higher selectivity or lower thickness requirements on the Cr mask. One positive aspect of the three-layer mask is that when etch times are with lax error margins, the etching of masks and target material can be done in just a single RIE session after mr-PosEBR is developed. This recipe can be enhanced further by researching other e-beam resists that can be made much thicker without sacrificing edge quality that much. There also should be room to tune the etch recipe of Al_2O_3 to increase selectivity between it and mr-PosEBR. Etching of Al_2O_3 should be indifferent to lower etch temperatures, which could be used to decrease the etch rate of mr-PosEBR. Post-baking of the resist could also be investigated to increase etch resistance.

Problems arose when trying to release $LiNbO_3$ platforms from SiO_2 with HF vapor etching. HF is not compatible at all with the metals used in the SINIS-junctions, but it was completely unexpected that there didn't seem to be a usable thickness for the Al_2O_3 layer to protect the junctions and still allow resistance measurements and bonding. Also, the mechanism of how HF can get around thinner Al_2O_3 layers to damage the junctions is a mystery as well. The initial guess is that evaporated Al_2O_3 is too grainy and thinner layers may leave gaps on the sides of metal leads even if it is evaporated from all sides evenly, which HF can exploit and attack metals.

A redesign of the fabrication process might be necessary if no easy solution is found to protect SINIS junctions in the HF vapor etch step. One possibility is to do HF etch first by etching very narrow slits on $LiNbO_3$ to allow HF vapor in and release part of the $LiNbO_3$ layer from SiO_2. Because the slits are narrow, resists could still be spun on $LiNbO_3$. Metallization would follow after the vapor etch. After metallization, a thick layer of PMMA would need to be spun as a cover before Cr could be evaporated as an $LiNbO_3$ etch mask. This Cr mask can be thick and also wet-etched as the gap would be etched while etching the slits. After wet etch, there is no need to develop the resist as burning through it could add a maximum of a few minutes more etch time. A big downside to the proposed technique is that alignment of the second etch mask is going to be difficult.

Calculations were done after experimental work was halted, and they showed in retrospect that initial samples were fabricated in the least optimal direction, Z-direction. The tunneling gap was aligned so that vacuum interfaces of both platforms would be Z-cuts. However, calculations showed that X-cut had the strongest flux, but Y-cut wasn't much far off. Therefore, any future samples with X-cut LNOI silicon chips should be aligned so that vacuum interfaces are Y-cut surfaces.

All in all, this thesis provided insight on new fabrication techniques on $LiNbO_3$ and some of those techniques could be used in other materials that require rough dry etching recipes. Numerical calculations were provided to better understand the tunneling phenomenon on $LiNbO_3$ and predict which crystal orientations should be investigated first. The results of this thesis and the phenomenon of phonon tunneling still warrant further investigation of $LiNbO_3$, despite the difficulties encountered in fabricating samples on LNOI silicon chips.

References

[1] M. Mitchell Waldrop. "The chips are down for Moore's law". In: *Nature* 530 (2016), pp. 144–147. DOI: doi:10.1038/530144a. URL: https://www.nature.com/news/the-chips-are-down-for-moore-s-law-1.19338.

[2] E. Pop, S. Sinha, and K.E. Goodson. "Heat Generation and Transport in Nanometer-Scale Transistors". In: *Proceedings of the IEEE* 94.8 (2006), pp. 1587–1601. DOI: 10.1109/JPROC.2006.879794.

[3] Biswajeet Guha et al. "Near-Field Radiative Cooling of Nanostructures". In: *Nano Letters* 12.9 (2012). PMID: 22891815, pp. 4546–4550. DOI: 10.1021/nl301708e. eprint: https://doi.org/10.1021/nl301708e. URL: https://doi.org/10.1021/nl301708e.

[4] Linxiao Zhu et al. "Near-field photonic cooling through control of the chemical potential of photons". In: *Nature* 566.7743 (Feb. 2019), pp. 239–244. ISSN: 1476-4687. DOI: 10.1038/s41586-019-0918-8. URL: https://doi.org/10.1038/s41586-019-0918-8.

[5] Steven H. Simon. *The Oxford Solid State Basics*. 1st ed. Oxford University Press, 2013. ISBN: 9780199680764. URL: http://gen.lib.rus.ec/book/index.php?md5=e60a88c9b121108e167197b3fde2e2a7.

[6] R. Paschotta. *Phonons*. RP Photonics Encyclopedia. Available online at https://www.rp-photonics.com/phonons.html. Mar. 2005. DOI: 10.61835/spa. URL: https://www.rp-photonics.com/phonons.html (visited on 02/08/2024).

[7] Zhuoran Geng. "Piezoelectrically mediated acoustic phonon tunneling". PhD thesis. Jyväskylä University, 2023. ISBN: 978-951-39-9533-1.

[8] Longfei Wang and Zhong Lin Wang. "Advances in piezotronic transistors and piezotronics". In: *Nano Today* 37 (2021), p. 101108. ISSN: 1748-0132. DOI: https://doi.org/10.1016/j.nantod.2021.101108. URL: https://www.sciencedirect.com/science/article/pii/S1748013221000335.

[9] Ted Belytschko, Wing Kam Liu, and Brian Moran. *Nonlinear Finite Elements for Continua and Structures*. 1st. Wiley, 2000. ISBN: 978-0471987734.

[10] B.A. Auld. *Acoustic fields and waves in solids*. A Wiley-Interscience publication. Wiley, 1973. ISBN: 9785885013437. URL: https://books.google.fi/books?id=_2MWAwAAQBAJ.

[11] Charles Kittel. *Introduction to Solid State Physics*. 8th ed. John Wiley & Sons, Inc, 2005. ISBN: 0-471-41526-X.

[12] Zhuoran Geng and Ilari J. Maasilta. "Acoustic wave tunneling across a vacuum gap between two piezoelectric crystals with arbitrary symmetry and orientation". In: *Phys. Rev. Res.* 4 (3 June 2022), p. 033073. DOI: 10.1103/PhysRevResearch.4.033073. URL: https://link.aps.org/doi/10.1103/PhysRevResearch.4.033073.

[13] D. M. Barnett and J. Lothe. "Dislocations and line charges in anisotropic piezoelectric insulators". In: *physica status solidi (b)* 67.1 (1975), pp. 105–111. DOI: https://doi.org/10.1002/pssb.2220670108. eprint: https://onlinelibrary.wiley.com/doi/pdf/10.1002/pssb.2220670108. URL: https://onlinelibrary.wiley.com/doi/abs/10.1002/pssb.2220670108.

[14] Zhuoran Geng and Ilari J. Maasilta. *Heat transfer across a vacuum gap induced by piezoelectrically mediated acoustic phonon tunneling*. 2023. arXiv: 2303.05084 [cond-mat.mes-hall].

[15] Zhuoran Geng and Ilari J. Maasilta. "Complete tunneling of acoustic waves between piezoelectric crystals". In: *Communications Physics* 6.1 (June 2023). ISSN: 2399-3650. DOI: 10.1038/s42005-023-01293-y. URL: http://dx.doi.org/10.1038/s42005-023-01293-y.

[16] R. S. Weis and T. K. Gaylord. "Lithium niobate: Summary of physical properties and crystal structure". In: *Applied Physics A*. 1432-0630 37 (4 Aug. 1985), pp. 191–203. DOI: 10.1007/BF00614817. URL: https://doi.org/10.1007/BF00614817.

[17] Jan Tichý et al. *Fundamental sof Piezoelectric SensoricsMechanical, Dielectric,and Thermodynamical Propertiesof Piezoelectric Materials*. springer, 2010. ISBN: 978-3-540-43966-0. DOI: 10.1007/978-3-540-68427-5.

[18] Di Zhu et al. *Integrated photonics on thin-film lithium niobate*. Feb. 2021. URL: https://www.researchgate.net/publication/349583295_Integrated_photonics_on_thin-film_lithium_niobate.

[19] Simone Sanna and Wolf Gero Schmidt. "Lithium niobate X-cut, Y-cut, and Z-cut surfaces from ab initio theory". In: *Phys. Rev. B* 81 (21 June 2010), p. 214116. DOI: 10.1103/PhysRevB.81.214116. URL: https://link.aps.org/doi/10.1103/PhysRevB.81.214116.

[20] S. Sanna et al. "Surface Charge of Clean LiNbO3 Z-Cut Surfaces". In: *High Performance Computing in Science and Engineering '14*. Ed. by Wolfgang E. Nagel, Dietmar H. Kröner, and Michael M. Resch. Cham: Springer International Publishing, 2015, pp. 163–178. ISBN: 978-3-319-10810-0.

[21] Simone Sanna and Wolf Gero Schmidt. "LiNbO3 surfaces from a microscopic perspective". In: *Journal of Physics: Condensed Matter* 29.41 (Sept. 2017), p. 413001. DOI: 10.1088/1361-648X/aa818d. URL: https://dx.doi.org/10.1088/1361-648X/aa818d.

[22] Sushmitha Vinikumar and Clarissa Schönecker. "Spreading dynamics on lithium niobate: An example of an intrinsically charged ferroelectric surface". In: *Colloids and Surfaces A: Physicochemical and Engineering Aspects* 673 (2023), p. 131792. ISSN: 0927-7757. DOI: https://doi.org/10.1016/j.colsurfa.2023.131792. URL: https://www.sciencedirect.com/science/article/pii/S0927775723008762.

[23] Tobias Jungk, Ákos Hoffmann, and Elisabeth Soergel. "Detection mechanism for ferroelectric domain boundaries with lateral force microscopy". In: *Applied Physics Letters* 89.4 (July 2006), p. 042901. ISSN: 0003-6951. DOI: 10.1063/1.2234303. eprint: {https://pubs.aip.org/aip/apl/article-pdf/doi/10.1063/1.2234303/13161134/042901_1_online.pdf}. URL: https://doi.org/10.1063/1.2234303.

[24] K.R. Williams, K. Gupta, and M. Wasilik. "Etch rates for micromachining processing-Part II". In: *Journal of Microelectromechanical Systems* 12.6 (2003), pp. 761–778. DOI: 10.1109/JMEMS.2003.820936.

[25] Vy Thi Hoang Nguyen et al. "Cr and CrOx etching using SF6 and O2 plasma". In: *Journal of Vacuum Science & Technology B* 39.3 (Apr. 2021), p. 032201. ISSN: 2166-2746. DOI: 10.1116/6.0000922. eprint: https://pubs.aip.org/

avs/jvb/article-pdf/doi/10.1116/6.0000922/13623807/032201_1_online.pdf. URL: https://doi.org/10.1116/6.0000922.

[26] Ozgur Yavuzcetin et al. "Photonic crystal fabrication in lithium niobate via pattern transfer through wet and dry etched chromium mask". In: *Journal of Applied Physics* 112.7 (Oct. 2012), p. 074303. ISSN: 0021-8979. DOI: 10.1063/1.4756958. eprint: https://pubs.aip.org/aip/jap/article-pdf/doi/10.1063/1.4756958/15099513/074303_1_online.pdf. URL: https://doi.org/10.1063/1.4756958.

[27] Stefan Pfirrmann et al. "mr-PosEBR: a novel positive tone resist for high resolution electron beam lithography and 3D surface patterning". In: *Advances in Patterning Materials and Processes XXXIII*. Ed. by Christoph K. Hohle and Rick Uchida. Vol. 9779. International Society for Optics and Photonics. SPIE, 2016, p. 977925. DOI: 10.1117/12.2219165. URL: https://doi.org/10.1117/12.2219165.

[28] Stefan Tegen and Peter Moll. "Etch Characteristics of Al2O3 in ICP and MERIE Plasma Etchers". In: *Journal of The Electrochemical Society* 152.4 (Mar. 2005), G271. DOI: 10.1149/1.1865912. URL: https://dx.doi.org/10.1149/1.1865912.

[29] Z. Ren et al. "Etching characteristics of LiNbO3 in reactive ion etching and inductively coupled plasma". In: *Journal of Applied Physics* 103.3 (Feb. 2008), p. 034109. ISSN: 0021-8979. DOI: 10.1063/1.2838180. eprint: https://pubs.aip.org/aip/jap/article-pdf/doi/10.1063/1.2838180/15003264/034109_1_online.pdf. URL: https://doi.org/10.1063/1.2838180.

[30] Tumura Masashi and Shinzo Yoshikado. "Etching characteristics of LiNbO3 crystal by fluorine gas plasma reactive ion etching". In: *Science and Technology of Advanced Materials* 2.3-4 (2001), pp. 563–569. DOI: 10.1016/S1468-6996(01)00138-3. eprint: https://doi.org/10.1016/S1468-6996(01)00138-3. URL: https://doi.org/10.1016/S1468-6996(01)00138-3.

[31] Takahiro Fujii and Shinzo Yoshikado. "Surface evaluation of LiNbO3 and LiTaO3 crystals etched using fluorine system gas plasma reactive ion etching". In: *Electrical Engineering in Japan* 149.2 (2004), pp. 18–24. DOI: https://doi.org/10.1002/eej.10365. eprint: https://onlinelibrary.wiley.

com/doi/pdf/10.1002/eej.10365. URL: https://onlinelibrary.wiley.com/doi/abs/10.1002/eej.10365.

[32] G. Ulliac et al. "Argon plasma inductively coupled plasma reactive ion etching study for smooth sidewall thin film lithium niobate waveguide application". In: *Optical Materials* 53 (2016), pp. 1–5. ISSN: 0925-3467. DOI: https://doi.org/10.1016/j.optmat.2015.12.040. URL: https://www.sciencedirect.com/science/article/pii/S0925346715301816.

[33] Fabian Kaufmann et al. In: *Nanophotonics* 12.8 (2023), pp. 1601–1611. DOI: doi:10.1515/nanoph-2022-0676. URL: https://doi.org/10.1515/nanoph-2022-0676.

[34] Juergen Soechtig et al. "Grating reflectors for erbium-doped lithium niobate waveguide lasers". In: *Nanofabrication Technologies and Device Integration*. Ed. by Wolfgang Karthe. Vol. 2213. International Society for Optics and Photonics. SPIE, 1994, pp. 98–107. DOI: 10.1117/12.180951. URL: https://doi.org/10.1117/12.180951.

[35] A. Witvrouw et al. "Comparison between wet HF etching and vapor HF etching for sacrificial oxide removal". In: *Proceedings of SPIE - The International Society for Optical Engineering* 4174 (Aug. 2000). DOI: 10.1117/12.396423.

[36] Thor Bakke et al. "Etch stop materials for release by vapor HF etching". In: *Proc. MicroMechanics Eur. Workshop* 16 (Jan. 2005).

[37] Heini Saloniemi and Mikko Tuohiniemi. "Study on Al2O3 film in anhydrous HF vapor". In: *Solid State Phenomena* 187 (Apr. 2012), pp. 45–48. DOI: 10.4028/www.scientific.net/SSP.187.45.

[38] R. Geiss et al. "Light propagation in a free-standing lithium niobate photonic crystal waveguide". In: *Applied Physics Letters* 97.13 (Sept. 2010), p. 131109. ISSN: 0003-6951. DOI: 10.1063/1.3496040. eprint: https://pubs.aip.org/aip/apl/article-pdf/doi/10.1063/1.3496040/13663744/131109_1_online.pdf. URL: https://doi.org/10.1063/1.3496040.